Article

MYC ecDNA promotes intratumour heterogeneity and plasticity in PDAC

https://doi.org/10.1038/s41586-025-08721-9

Received: 6 October 2023

Accepted: 30 January 2025

Published online: 12 March 2025

Open access

Check for updates

Elena Fiorini[1,19], Antonia Malinova[1,19], Daniel Schreyer[2,19], Davide Pasini[1,3], Michele Bevere[4], Giorgia Alessio[1,3], Diego Rosa[1,3], Sabrina D'Agosto[4,17], Luca Azzolin[5], Salvatore Milite[5], Silvia Andreani[4,18], Francesca Lupo[1], Lisa Veghini[1], Sonia Grimaldi[4], Serena Pedron[6], Monica Castellucci[7], Craig Nourse[8,9], Roberto Salvia[10], Giuseppe Malleo[10], Andrea Ruzzenente[11], Alfredo Guglielmi[11], Michele Milella[12], Rita T. Lawlor[1,4], Claudio Luchini[6], Antonio Agostini[13,14], Carmine Carbone[13], Christian Pilarsky[15], Andrea Sottoriva[5], Aldo Scarpa[4,6], David A. Tuveson[16], Peter Bailey[2,9,20] ✉ & Vincenzo Corbo[1,4,20] ✉

Intratumour heterogeneity and phenotypic plasticity drive tumour progression and therapy resistance[1,2]. Oncogene dosage variation contributes to cell-state transitions and phenotypic heterogeneity[3], thereby providing a substrate for somatic evolution. Nonetheless, the genetic mechanisms underlying phenotypic heterogeneity are still poorly understood. Here we show that extrachromosomal DNA (ecDNA) is a major source of high-level focal amplification in key oncogenes and a major contributor of *MYC* heterogeneity in pancreatic ductal adenocarcinoma (PDAC). We demonstrate that ecDNAs drive varying levels of *MYC* dosage, depending on their regulatory landscape, enabling cancer cells to rapidly and reversibly adapt to microenvironmental changes. In the absence of selective pressure, a high ecDNA copy number imposes a substantial fitness cost on PDAC cells. We also show that MYC dosage affects cell morphology and dependence of cancer cells on stromal niche factors. Our work provides a detailed analysis of ecDNAs in PDAC and describes a new genetic mechanism driving *MYC* heterogeneity in PDAC.

Oncogene dosage variation is a major determinant of tumour progression and phenotypic heterogeneity[1–3]. Focal oncogene amplifications and rearrangements have been demonstrated to underpin oncogene dosage variation and can exist as linear amplifications of contiguous genomic segments or as ecDNAs. ecDNAs lack centromeres and therefore segregate unevenly between daughter cells during mitosis[4,5]. This non-Mendelian pattern of inheritance enables individual cells to accumulate large numbers of ecDNA-bearing oncogenes in response to specific microenvironmental changes[6]. Rapid depletion of ecDNAs is also observed when cancer cells are no longer exposed to the selective pressure for which they confer enhanced fitness[6–9].

Oncogenic amplifications of genes including *GATA6*, *KRAS* and *MYC* have been shown to shape PDAC cancer phenotypes[3,10–14]. Elevated *MYC* activity promotes biologically aggressive PDAC phenotypes by driving proliferation and remodelling of the tumour microenvironment[15,16]. *MYC* amplifications are specifically enriched in PDAC liver metastases and are associated with basal-like and squamous subtypes[15]. Therefore, the identification of genetic events that drive *MYC* transcriptional heterogeneity is critical to advance our understanding of disease progression and metastasis. To overcome the limitation of poor neoplastic cellularity of PDAC tissues and to robustly map the dynamic genomic changes associated with endogenous oncogene amplifications, we comprehensively characterized a large panel of patient-derived organoids (PDOs). The integration of PDO genomes, transcriptomes and in situ analyses with functional studies have revealed the role of ecDNA-based *MYC* amplification in driving extensive copy number heterogeneity, and the morphological and phenotypical adaptation of PDAC cells to the depletion of stromal niche factors.

ecDNA-driven oncogene amplification in PDAC

To characterize the genomic rearrangements that underpin copy number variation in PDAC, we performed whole-genome sequencing (WGS) on 41 early passage PDOs established from 39 primary tumours (Supplementary Table 1).

Consistent with earlier studies[17–19], PDOs exhibited frequent copy number alterations in canonical PDAC genes, including copy number loss of *CDKN2A*, *TP53* and *SMAD4* and copy number gains in *KRAS* and

[1]Department of Engineering for Innovation Medicine, University of Verona, Verona, Italy. [2]School of Cancer Sciences, University of Glasgow, Glasgow, UK. [3]Department of Medicine, University of Verona, Verona, Italy. [4]ARC-Net Research Centre, University of Verona, Verona, Italy. [5]Computational Biology Research Centre, Human Technopole, Milan, Italy. [6]Department of Diagnostics and Public Health, University of Verona, Verona, Italy. [7]Centro Piattaforme Tecnologiche, University of Verona, Verona, Italy. [8]Cancer Research UK Beatson Institute, Glasgow, UK. [9]Botton-Champalimaud Pancreatic Cancer Centre, Lisbon, Portugal. [10]Department of General and Pancreatic Surgery, The Pancreas Institute, University of Verona, Verona, Italy. [11]Department of Surgical Sciences, Division of General and Hepatobiliary Surgery, University of Verona, Verona, Italy. [12]Section of Medical Oncology, Department of Medicine, University of Verona, Verona, Italy. [13]Department of Medical and Surgical Sciences, Fondazione Policlinico Universitario Agostino Gemelli IRCCS, Rome, Italy. [14]Bioinformatics Research Core Facility, Gemelli Science and Technology Park (GSTeP), Rome, Italy. [15]Department of Surgery, Universitätsklinikum Erlangen, Erlangen, Germany. [16]Cold Spring Harbor Laboratory, Cold Spring Harbor, NY, USA. [17]Present address: Human Technopole, Milan, Italy. [18]Present address: Department of Biochemistry and Molecular Biology, University of Würzburg, Würzburg, Germany. [19]These authors contributed equally: Elena Fiorini, Antonia Malinova, Daniel Schreyer. [20]These authors jointly supervised this work: Peter Bailey, Vincenzo Corbo. ✉e-mail: peter.bailey@research.fchampalimaud.org; vincenzo.corbo@univr.it

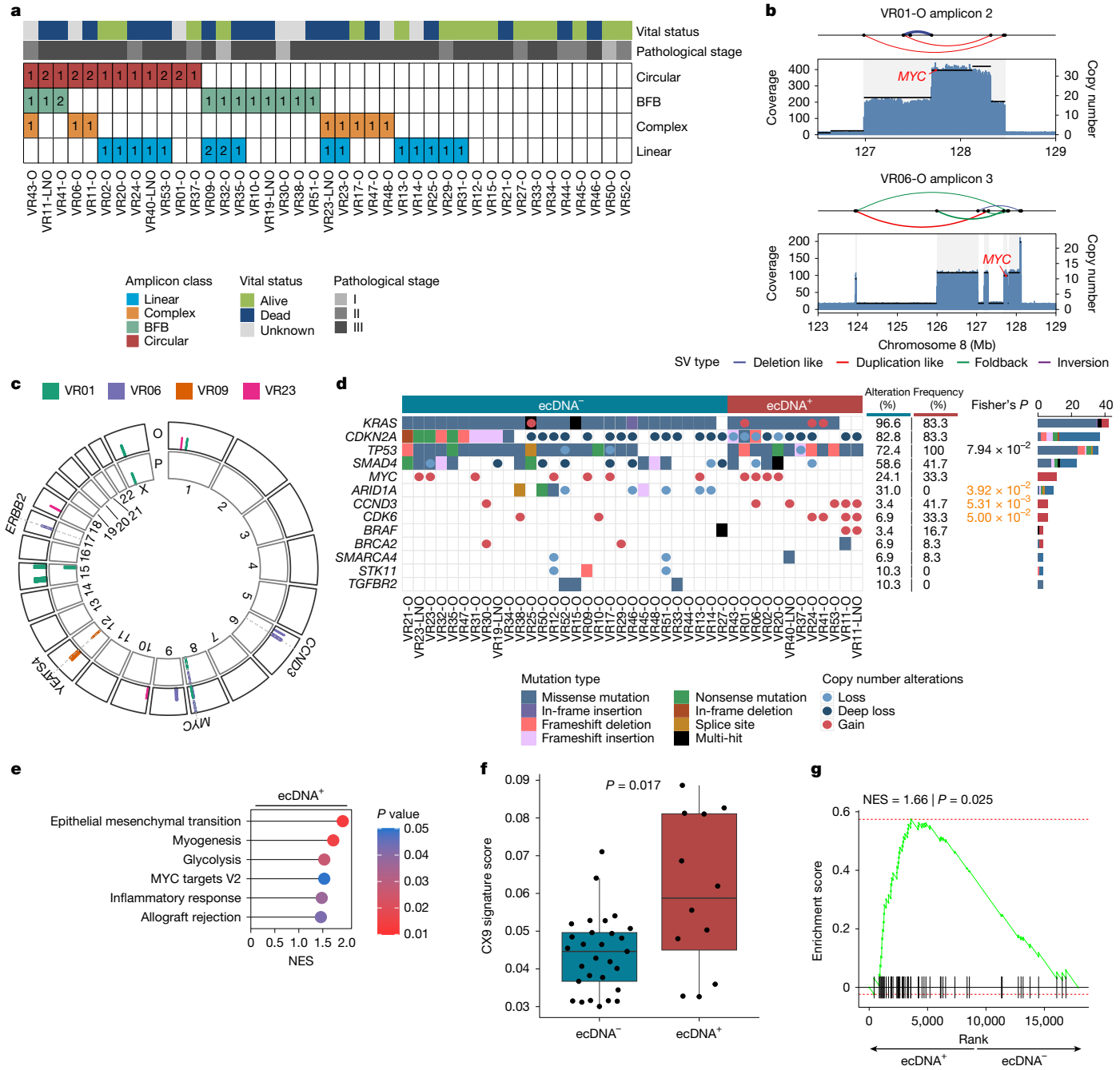

Fig. 1 | Gene amplification landscape of PDAC. a, AmpliconArchitect-based classification of PDOs. The number of amplicons for each sample is indicated. The pathological stage of patients at time of resection and the vital status at follow-up are colour coded. **b**, Genomic view of AmpliconArchitect-reconstructed amplicon structures spanning the *MYC* locus for the organoids with *MYC* ecDNA. Coverage depth, copy number segments and structural variant (SV) connections are shown. **c**, Circular plot showing amplicon regions identified in primary tumours (P) from four patients are retained in the matched organoids (O). **d**, Oncoplot showing the altered genes in PDOs classified as ecDNA$^+$ (red) and ecDNA$^-$ (blue). The types of alterations are colour and shape coded. Gain denotes copy number ≥3, loss indicates copy number ≤1, and deep loss refers to copy number ≤ 0.25. Fisher's exact test (two-sided) was used to identify associations between genomic alterations in specific genes and ecDNA status. $P < 0.1$ is displayed, and significance ($P < 0.05$) is highlighted in orange. **e**, Lollipop plot showing gene set enrichment analysis on Hallmark pathways significantly enriched in ecDNA$^+$ PDOs ($n = 7$) compared with ecDNA$^-$ PDOs ($n = 7$). The *P* value was calculated using the multilevel splitting Monte Carlo approach. NES, normalized enrichment score. **f**, Boxplot showing the CX9 chromosomal instability signature enriched in ecDNA$^+$ PDOs. The boxplots show the median (centre line), upper and lower quartiles (box limits), and 1.5× interquartile range (whiskers). $n = 29$ PDOs (ecDNA$^-$) and $n = 12$ PDOs (ecDNA$^+$). Statistical significance was evaluated using a two-sided Wilcoxon rank-sum test. **g**, Gene set enrichment analysis of differentially expressed genes between ecDNA$^+$ ($n = 7$) and ecDNA$^-$ ($n = 7$) PDOs in the CIN70 transcriptomic signature. The *P* value was calculated using the multilevel splitting Monte Carlo approach. The red dashed lines indicate the maximum and the minimum of the enrichment score.

MYC (Extended Data Fig. 1a). AmpliconArchitect[20] was used to reconstruct genomic regions associated with high copy number gains, classifying them as either linear, break-fusion-bridge (BFB), complex or ecDNA amplicons (Fig. 1a and Supplementary Table 2). This analysis revealed that 12 out of 41 PDOs had at least one distinct ecDNA (Fig. 1a). The identification of ecDNAs in PDOs is consistent with earlier WGS

analyses derived from resected material from patients with PDAC[21]. We observed higher fractions of tumour-bearing amplifications in PDOs (Human Cancer Model Initiative (HCMI)) than in primary tumours (International Cancer Genome Consortium (ICGC); 73.17% versus 66.1%), including ecDNA amplifications (29.3% versus 14.2%), which may be due to increased detection in pure neoplastic populations (Extended Data Fig. 1b,c).

CCND3 and *MYC* were the most recurrently amplified genes in our cohort of PDOs, whereas linear amplicons were the most commonly AmpliconArchitect-reconstructed amplicon type (Fig. 1a). Amplifications of *CCND3* were identified in 6 out of 41 PDOs and described as either circular, BFB or complex amplicons (Extended Data Fig. 1d). Amplifications of *MYC* were identified in 11 PDOs with 2 PDOs harbouring *MYC* on ecDNA (Fig. 1b). Circularization for in vitro reporting of cleavage effects by sequencing (CIRCLE-seq)[22] validated the circular amplicon containing *MYC* in VR01 organoid (VR01-O) (Extended Data Fig. 1e). *MYC* ecDNAs were derived from contiguous genomic regions on chromosome 8 comprising *MYC* and adjacent genes *PVT1* and *CASC11* (Extended Data Fig. 1f and Supplementary Table 2). Circular amplicon breakpoints for the two *MYC* ecDNAs were further validated by capillary sequencing (Extended Data Fig. 1g,h).

AmpliconArchitect analysis of four primary PDAC samples with matched PDOs demonstrated that the structure of *MYC* ecDNA amplicons between parental tissue and derived PDOs were concordant (Fig. 1c and Extended Data Fig. 1i).

To link patterns of ecDNA gene amplification to key mutational drivers, we performed high-coverage targeted sequencing (Supplementary Table 3). PDOs containing ecDNAs displayed biallelic inactivation of *TP53* (Fig. 1d) and were enriched for copy number loss of *CDKN2A* on chromosome 9 and for copy number gains on chromosome 6 (*CCND3*) and chromosome 7 (*CDK6*; Fig. 1d and Extended Data Fig. 2a). Moreover, the presence of an ecDNA inversely correlated with inactivating TGFβ pathway alterations (Extended Data Fig. 2b). Whole-genome duplications were more frequent in PDOs harbouring ecDNA (Extended Data Fig. 2c). Consistent with earlier findings[23,24], genes on ecDNAs exhibited significantly elevated levels of expression when compared with those on other amplicon types (Extended Data Fig. 2d).

Gene expression programmes commonly linked to biologically aggressive tumours, such as epithelial-to-mesenchymal transition and glycolysis, were significantly enriched in ecDNA PDOs ($n = 7$) compared with non-ecDNA PDOs ($n = 7$; Fig. 1e and Supplementary Table 4). ecDNA$^+$ PDOs were also enriched for copy number signatures defining patterns of mid-level amplifications, which have been associated with replication stress (CX9)[25] (Fig. 1f). Endogenous replication stress can cause genomic instability, which in turn may result in ecDNA formation[26]. Consistent with this idea, ecDNA$^+$ PDOs showed enrichment for a transcriptomic signature (CIN70) of chromosomal instability[27] (Fig. 1g). Overall, we found a heterogeneous landscape of genomic amplifications in PDOs and that ecDNA tumours display features of more biologically aggressive disease.

MYC ecDNA-driven intratumour heterogeneity

To explore how ecDNA contributes to PDAC intratumour heterogeneity, we examined *MYC* amplifications as either extrachromosomal (ec*MYC*) or linear intrachromosomal (ic*MYC*). High-level *MYC* amplifications in our cohort were predicted to reside on ecDNAs (Extended Data Fig. 3a), with significantly higher *MYC* expression in ecDNA-bearing cultures (Extended Data Fig. 3b).

DNA FISH for *MYC* and Centromere 8 (*CEN8*) on metaphase spreads from the three ic*MYC* PDOs revealed no MYC-positive ecDNAs (Extended Data Fig. 3c). By contrast, ten to hundreds of individual *MYC*-positive ecDNA per nucleus were observed in metaphases prepared from the ec*MYC* PDOs (VR01 and VR06; Fig. 2a). Next, we examined interphase nuclei to observe the spatial organization of FISH-positive signals and estimate the cell-to-cell variation for the number of *MYC* copies. Interphase FISH signals were mostly confined to specific regions of the nucleus in ecDNA-bearing cultures (Fig. 2b). Quantification of interphase FISH signals in ecDNA PDOs using autocorrelation[28] showed a significant increase of signals clustering over short range compared with random distribution for both VR01 and VR06 (Fig. 2c). The two ecDNA-bearing cultures exhibited the greatest variability in both *MYC* copy number and oncogene expression (Fig. 2b and Extended Data Fig. 3b,c). Substantial variability of *MYC* copy number states was even observed in individual organoids (Fig. 2d). VR01-O displayed the highest average copy number count, with a few cells carrying hundreds of ecDNA molecules (Fig. 2b). However, after normalizing by copy number, VR06-O exhibited the highest *MYC* expression and VR01-O the lowest among all the PDOs considered (Extended Data Fig. 3d). This suggested the presence of regulatory elements on the VR01-O circular amplicon limiting *MYC* expression.

A known tumour suppressor element that acts in *cis* to reduce *MYC* expression is the promoter of the long-non-coding RNA *PVT1* (ref. 29). The AmpliconArchitect-predicted structure for the *MYC* ecDNA in VR06-O lacked the promoter and the first exons of *PVT1* (Fig. 2e). These elements were instead retained in the predicted structure of the ecDNA in VR01-O, thereby providing an explanation for the supercharged *MYC* expression in VR06-O compared with VR01-O. Consistent with the promoter–enhancer competition mechanisms between *MYC* and *PVT1*, *PVT1* expression was higher than that of *MYC* in VR01-O but not in VR06-O (Fig. 2e).

We then analysed the primary tissues from which the PDOs were established and confirmed the significant cell-to-cell variation of *MYC* FISH foci in the ecDNA-bearing tumours (Fig. 2f) as well as higher MYC expression at the protein level (Extended Data Fig. 3e). Together, our data indicate that ecDNAs contribute to significant copy number and transcriptional intratumour heterogeneity in PDAC. We also find that the transcriptional output does not scale linearly with ecDNA copy number and that the structure of the ecDNA, that is, its regulatory landscape, has a major role in modulating gene expression.

MYC drives tumour adaptation to WNT-deficient niches

Next, we sought to understand how oncogene-bearing ecDNAs respond dynamically to microenvironmental cues to enhance the environmental fitness of PDAC cells. Previous studies have shown that not all PDAC cells withstand a WNT-deficient environment, and that acquisition of WNT independency is associated with disease progression[17,30,31]. To impose selective pressure, we removed WNT3A and RSPO (WR) from PDO growth media and tested survival of several cultures (Extended Data Fig. 4a). None of the PDOs tested ($n = 9$) survived continuous passaging (once per week) in WNT-depleted medium (−WR; Extended Data Fig. 4a), confirming this as a hostile environmental condition for PDOs. *MYC* is a well-established WNT pathway target gene[32] and *MYC* expression was rapidly induced in PDOs treated with WNT agonists (Extended Data Fig. 4b). Therefore, we tested whether increased *MYC* dosage could bypass the need for exogenous WNT. Indeed, MYC overexpression was sufficient to eliminate the requirement for exogenous WR (Extended Data Fig. 4c,d). Furthermore, MYC-overexpressing cultures were completely insensitive to the porcupine inhibitor C59 (Extended Data Fig. 4e), which blocks endogenous WNT ligand production. The cultures were therefore considered as WR independent (WRi)[30,31]. These results implicate *MYC* as an important driver of WNT-gated survival in PDOs.

Considering the intraculture variability of ecDNA states, we rechallenged the PDOs (two ec*MYC*, three ic*MYC* and one *MYC* wild-type cultures) with WNT-depleted medium, this time without passaging cells until WRi phenotypes emerged. This approach probably favours the selection of a pre-existing population of WRi cells, allowing for comparison across replicates to distinguish between reproducible

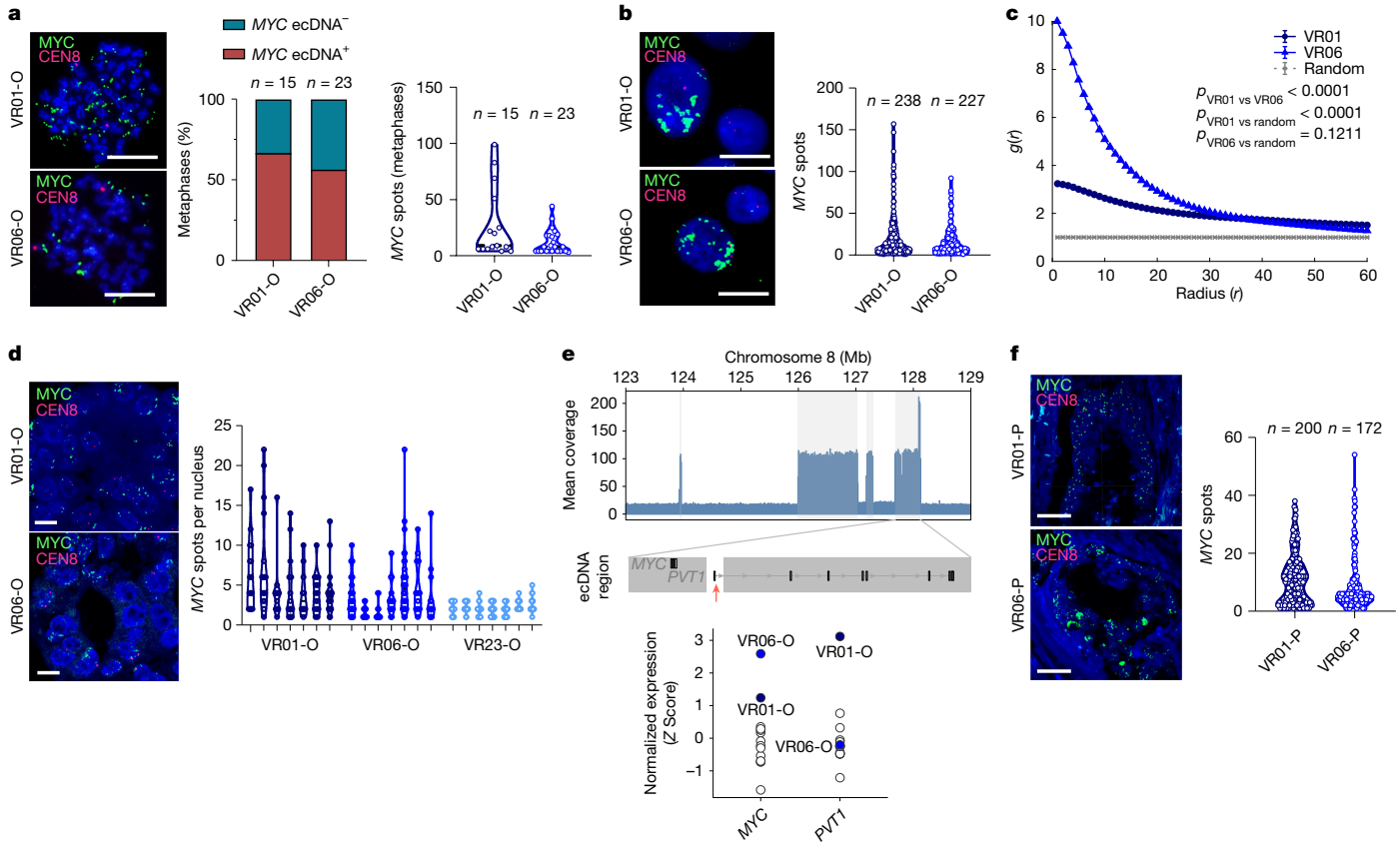

Fig. 2 | ecDNAs promote intratumour heterogeneity of *MYC* copy number in PDAC. a, Representative FISH images validating the presence of *MYC* on ecDNA in VR01 and VR06 PDOs (left). Scale bars, 20 µm. The stacked barplot displays the frequency of ecDNA$^+$ metaphases in VR01-O ($n = 15$) and VR06-O ($n = 23$) (middle). Quantification of *MYC* signals per metaphase (as a proxy for ecDNA copy number) in VR01-O and VR06-O (right). **b**, Representative FISH images of interphase nuclei of VR01-O and VR06-O (left). Scale bars, 20 µm. Quantification of *MYC* signals per nucleus as a proxy for ecDNA copy number in VR01-O ($n = 238$) and VR06-O ($n = 227$) (right). **c**, Interphase signal clustering by autocorrelation $g(r)$[28]. The *P* values were determined by two-sided Wilcoxon test at $r = 0$ compared with random distribution (grey). **d**, Representative FISH images of ec*MYC*-embedded organoids (left). Scale bars, 10 µm. Histograms show the distribution of *MYC* signals per cell in seven individual organoids from VR01-O, VR06-O and VR23-O (right). **e**, Genomic view of VR06 ec*MYC* segments (top; highlighted in grey) and the location of *MYC* and *PVT1*. The *PVT1* starting region is absent on the VR06 ec*MYC* (arrow) (middle). *MYC* and *PVT1* normalized expression values (*Z* score) of the two ec*MYC* PDOs (blue) compared with non-ecDNA-bearing cultures (white) (bottom). **f**, Representative FISH images of VR01 primary (VR01-P) and VR06-P tissues (left). Scale bars, 40 µm. Quantification of *MYC* spots per nucleus of VR01-P ($n = 200$) and VR06-P ($n = 172$) (right).

versus stochastic evolutionary dynamics[33]. At these time points, ecDNA dynamics were assessed using a combination of WGS, FISH and droplet digital quantitative PCR (ddPCR) assays targeting the *MYC* locus and ecDNA breakpoints (see Methods; Extended Data Fig. 4f).

The withdrawal of WR from the medium led to the extinction of three cultures, including two with low-level copy number gains of *MYC* (VR02 and VR20). Conversely, WRi cultures consistently emerged from the two ec*MYC* and one ic*MYC* (Fig. 3a). The kinetics of the WRi phenotype emergence varied among different cultures but were consistent across replicates for the three cultures (Fig. 3b). Following WRi emergence, all cultures exhibited a similar pattern of exponential growth (Extended Data Fig. 4g), indicative of a fully adapted phenotype. Conversely, a high-passage VR06-O, which had completely lost ecDNA, did not survive WNT withdrawal, with no evidence for the generation of ecDNA-containing *MYC* (Extended Data Fig. 4h).

To distinguish between adaptation and selection as mechanisms of WRi acquisition, we transduced each parental PDO with a library of 1 million random barcodes. To ensure one barcode per cell, 500,000 single cells were infected at a multiplicity of infection of 0.1, and then expanded into organoids. Each PDO culture incorporated between 3,000 and 4,000 unique barcodes, ensuring high barcode diversity (Fig. 3c). Two to three replicates per culture were subsequently seeded in WR-depleted medium until emergence of the WRi phenotype. In all cultures, the acquisition of the WRi phenotype was associated with a reduction of barcode diversity and a significant expansion of barcodes in VR01-O and VR23-O, but not in VR06-O (Fig. 3c). In the two biological replicates of VR01-O, the same subclone massively expanded, suggesting that evolution under these conditions is highly predictable for this organoid culture.

Environmental-induced selection of ecDNA

Integrated analysis of genomic and transcriptomic data ruled out that PDOs adaptation to WR withdrawal involved alternative activation of the WNT pathway in the two ecDNA$^+$ PDOs studied (Extended Data Fig. 4i–m and Supplementary Table 5). None of the WRi PDOs showed genetic alterations in WNT pathway regulators (Extended Data Fig. 4i). Furthermore, canonical WNT target gene expression (for example, *CLND2*, *LGR5*, *AXIN2* and *BMP4*) was significantly reduced or suppressed in ecDNA-bearing PDOs (Extended Data Fig. 4j–m). Finally, WRi cultures demonstrated no sensitivity to porcupine inhibition, indicating that adaptation was not driven by autocrine WNT ligand secretion (Extended Data Fig. 4n). To determine how microenvironmental stress affected chromosomal and extrachromosomal *MYC* dynamics, we initially applied AmpliconArchitect to WGS data obtained from two WRi PDO cultures (Extended Data Fig. 5a).

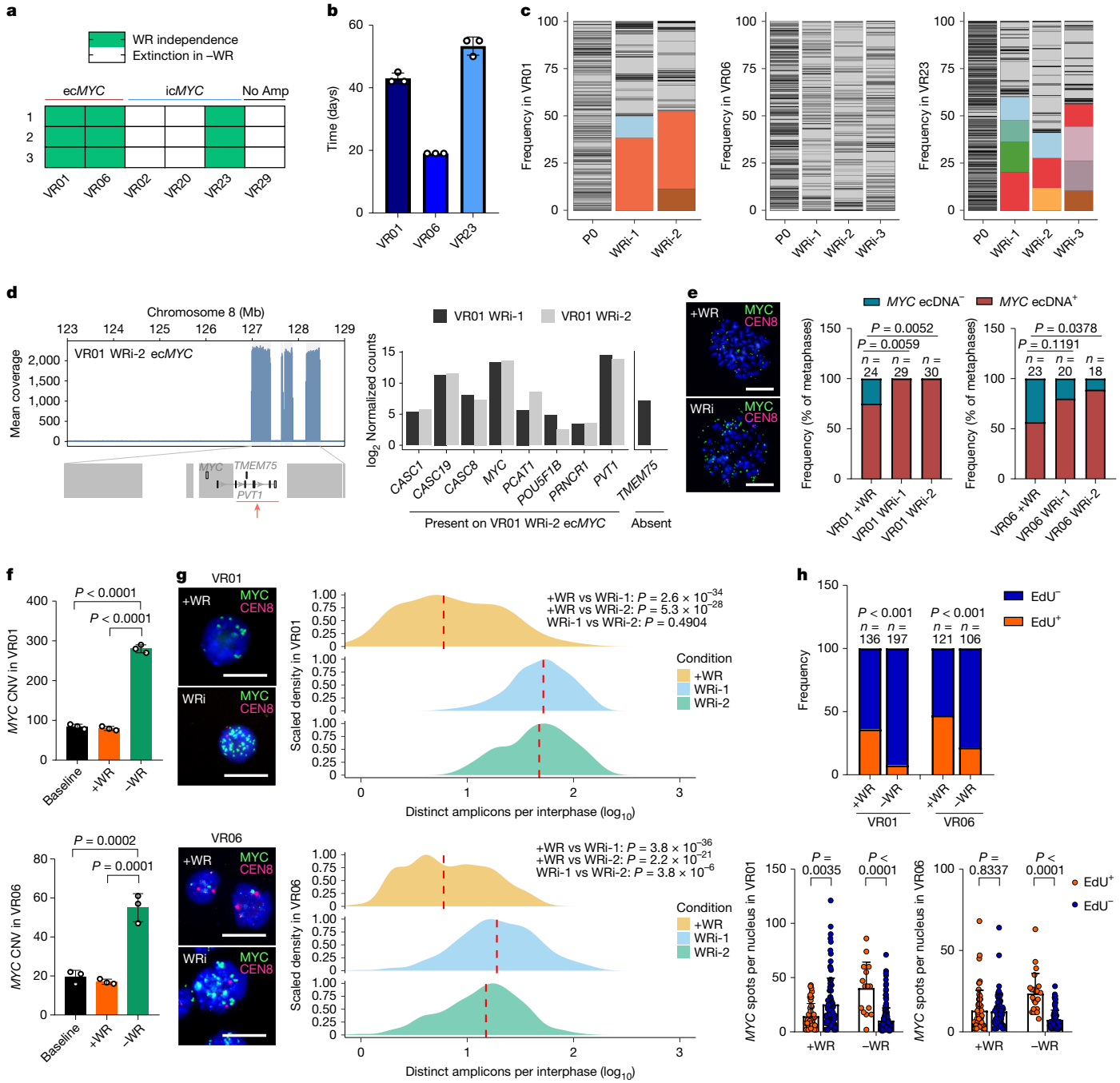

Fig. 3 | ec*MYC* promotes adaptation to niche factor withdrawal. a, PDOs, classified by MYC status, acquired independence from WNT agonists (WR; green; three independent repetitions). Amp, amplification. **b**, Days to WRi phenotype. Data are mean ± s.d. from three experiments. **c**, Lentiviral barcode proportions quantified from genomic DNA. Barcodes with a frequency above 10% are coloured. P0, parental culture. **d**, Structural difference between putative ecDNAs in VR01 WRi-1 and VR01 WRi-2 (left), and expression of genes on the ecDNAs (right). **e**, Metaphase FISH signals before (+WR) and after WRi emergence in VR01 (left). Scale bars, 20 µm. *MYC* ecDNA$^+$ metaphase frequency at baseline (VR01 $n = 24$ and VR06 $n = 23$) and after WRi (two biological replicates; VR01 WRi-1 $n = 29$, VR01 WRi-2 $n = 30$, VR06 WRi-1 $n = 20$ and VR06 WRi-2 $n = 18$) (right). The *P* value was calculated using Fisher's exact two-sided test. **f**, *MYC* copy number by ddPCR at baseline and following culture with (+WR) or without (−WR) WNT agonists. Data are mean ± s.d. of three biological replicates. The *P* value was calculated using one-way analysis of variance with Tukey's multiple comparisons test. CNV, copy number variation. **g**, Interphase FISH signals before (+WR) and after WRi (left). Scale bars, 20 µm. The copy number measured by interphase FISH of 103 and 308 nuclei for VR01 (top right) and VR06 (bottom right), respectively, at baseline (+WR). For WRi cultures, VR01 WRi-1 $n = 192$, VR01 WRi-2 $n = 136$, VR06 WRi-1 $n = 296$ and VR06 WRi-2 $n = 341$. The *P* values were determined by Wilcoxon rank-sum two-sided test. The red dashed line indicates the median copy number state. **h**, EdU$^+$ and EdU$^-$ nucleus frequency in PDOs cultivated with (+WR) or without (−WR) WNT agonists (top). The *P* values were determined by Fisher's exact two-sided test. *MYC* copies per nucleus stratified by EdU status (bottom). Data are mean ± s.d. The *P* values were determined by two-tailed Student's *t*-test. Quantifications summarize the data from one experiment; nuclei analysed: VR01 +WR $n = 136$, VR01 −WR $n = 197$, VR06 +WR $n = 121$ and VR06 −WR $n = 106$.

ecDNA containing *MYC* persisted in WRi PDOs, increased their integer copy number, and in one instance evolved its structure (Fig. 3d). No circular amplicons were found in VR23-O (ic*MYC* PDO; Extended Data Fig. 5a). The AmpliconArchitect-reconstructed circular amplicons for the adapted VR06-O were highly concordant with the circular amplicon described for the parental culture (Extended Data Fig. 5b).

Compared with the circular amplicon described in the parental culture of VR01-O and persisting in one of the WRi PDO, an individual genomic locus (*TMEM75*) was not included in the ecDNA structure described in VR01 WRi-2 (Fig. 3d). Accordingly, RNA sequencing did not detect expression of *TMEM75* in the corresponding PDO (Fig. 3d).

Consistent with positive selection for *MYC*-containing ecDNA, WRi PDOs exhibited a statistically significant increase in ecDNA$^+$ cell fraction (Fig. 3e), mean *MYC* copy number (Fig. 3f) and the number of ecDNA molecules per cell (Fig. 3g). *MYC* copy number changes in ecDNA$^+$ cultures were attributed to ecDNAs as shown by the ddPCR measure of both *MYC* copies and circular amplicons (Extended Data Fig. 5c). The mean *MYC* copy number of cultures grown in parallel without the selective pressure (+WR) remained consistent with the initial ecDNA copy number, suggesting that ecDNAs are under neutral selection in these conditions (Fig. 3f and Extended Data Fig. 5c). As expected for a fitness advantage in cells with elevated *MYC* copy number, upon WR withdrawal, the fraction of proliferating (EdU$^+$) cells in parental cultures was enriched with *MYC*^{high} cells (Fig. 3h). Of note, under unperturbed conditions (+WR), cells with extremely high *MYC* copy numbers were enriched in the non-proliferative fraction of VR01-O (Fig. 3h). In the ic*MYC* PDO, WRi was linked to either a mild increase in *MYC* copy number (VR23 WRi-1) or chromosome 8 polysomy (VR23 WRi-2) without changes in ploidy (Extended Data Fig. 5d,e). MYC upregulation at mRNA and protein levels was consistent with increased copy number and was more pronounced in ec*MYC* than in ic*MYC* PDOs (Extended Data Fig. 5f,g). RNA sequencing analysis of parental and adapted ec*MYC* PDOs revealed that increased mRNA expression of most ecDNA-encoded genes mirrored the ecDNA copy number gains (Extended Data Fig. 5h). However, owing to structural differences in ecDNAs (Fig. 2e), the magnitude of *MYC* and other gene expression changes did not always align with predicted copy number increases (Extended Data Fig. 5h).

Maintenance of ec*MYC* in PDAC organoids

In our culture system, acquisition of WRi was invariably associated with increased per cell content of ecDNA (Fig. 3g). ecDNA-driven cancer cells have been shown to display increased levels of phosphorylated histone H2AX (γH2AX)[26], which is required for the assembly of DNA damage response as well as for the activation of checkpoint proteins, which might arrest cell-cycle progression[34]. Moreover, antineoplastic treatments known to activate the DNA damage-sensing machinery have been shown to promote the loss of ecDNA through as yet uncharacterized mechanisms[35–37].

In PDOs, γH2AX levels were higher in cultures with increased ecDNA copy number (Extended Data Fig. 6a). In individual cultures, MYC protein expression positively and significantly correlated with *MYC* copy number (Extended Data Fig. 6b). Using MYC levels as a proxy for ec*MYC* copy number, we found that γH2AX foci were particularly prominent in *MYC*^{high} nuclei and MYC expression positively correlated with the intensity of γH2AX staining exclusively in ecDNA$^+$ cultures (Fig. 4a).

The forced overexpression of *MYC* through a lentiviral vector and the subsequent exposure of the cultures to WR-depleted medium led to a rapid decrease in *MYC* ecDNA molecules per cell (Extended Data Fig. 6c,d), sustained MYC expression (Fig. 4b), but not to increased levels of γH2AX (Fig. 4b). Similarly, the WRi ic*MYC* PDOs did not show increased levels of γH2AX (Fig. 4b and Extended Data Fig. 6e).

To directly assess whether a high ecDNA burden represents a fitness cost in the absence of a selective pressure, we reintroduced WR in the culture medium of WRi PDOs and evaluated ecDNA dynamics, as well as the fitness of cancer cells based on *MYC* copy number states.

As expected, in WNT-depleted medium, *MYC*^{high} cells were overrepresented in the active proliferating cell fraction (Fig. 4c). The exposure of the cultures to WNT-containing medium for 3 days was sufficient to reveal the reduced fitness of *MYC*^{high} cells, as these cells became significantly enriched in the non-proliferative fraction (Fig. 4c).

Longer exposure to WR-supplemented medium (approximately 30 days) resulted in a significant decrease in the fraction of ecDNA$^+$ cells (Fig. 4d), accompanied by a corresponding reduction in both the mean *MYC* copy number and the number of ecDNA molecules per cell (Fig. 4e,f).

Elimination of ecDNA can occur through the integration of an ecDNA into a chromosomal location to form a homogeneously staining region (HSR)[8,38,39], which is considered as a latent reservoir of ecDNAs. The number of HSR$^+$ cells only slightly increased for VR01-O, suggesting either integration of ecDNA into chromosomes or the enrichment for a pre-existing HSR$^+$ clone (Extended Data Fig. 6f). The reduction of ecDNA copies due to the removal of the imposed selection was associated with reduced levels of γH2AX (Extended Data Fig. 6g). Together, our results suggest a fitness cost for the maintenance of an elevated ecDNA burden in PDOs unless providing a survival advantage.

ecDNAs and cell phenotypes in PDAC

We then evaluated the phenotypic effects of ecDNA accumulation in PDAC organoids. WRi PDOs bearing ec*MYC* and high MYC expression showed distinct morphological changes shifting from a cystic-like structure to a solid or cribriform growth pattern, unlike ic*MYC* PDOs (Extended Data Fig. 7a). These cytoarchitectural features have previously been linked to basal-like/squamous commitment by cancer cells[30] regardless of WR supplementation in the medium and therefore have been proposed to reflect cell-intrinsic properties[30]. Along with the reduction of ecDNA molecules per cell, the removal of the selective pressure rapidly reversed morphological changes observed in ecDNA$^+$ WRi cultures (Extended Data Fig. 7b). By contrast, MYC-overexpressing cultures retained solid or cribriform growth patterns despite the neutralization of the selective pressure (Extended Data Fig. 7c).

Next, we evaluated whether ec*MYC* accumulation affected the cell states of the WRi PDOs. The accumulation of ec*MYC* was associated with predictable changes in transcriptomes across replicates (Extended Data Fig. 7d). Overall, the accumulation of ec*MYC* strengthened the classical and the basal programs[40,41] in VR01-O and VR06-O, respectively (Extended Data Fig. 7e). Conversely, adaptation of ic*MYC* PDO to WR withdrawal was associated with less predictable changes across replicates and accordingly more variable changes in cell state (Extended Data Fig. 7f). Changes in transcriptional cell states were concordant with immunophenotypic data, with the PDOs displaying the highest *MYC* dosage (VR06) showing expression, although heterogeneous, of squamous markers (CK5 and ΔNp63) and reduction of the classical marker GATA6 than the parental culture (Extended Data Fig. 7g,h).

Consistent with previous studies[28,42], targeting of *MYC* transcription via the BRD4 inhibitor JQ1 (ref. 43) significantly reduced *MYC*–ecDNA hubs (Extended Data Fig. 7i), lowered *MYC* mRNA levels especially in VR06-O WRi (Extended Data Fig. 7j), and preferentially reduced cell viability of ec*MYC* PDOs over ic*MYC* PDO (Extended Data Fig. 7k).

Spatial profiling of ecDNA-driven *MYC* in PDAC

To investigate the spatial context of ecDNA-driven *MYC* amplifications in vivo, we integrated spatial transcriptomics and cytogenetics on formalin-fixed, paraffin-embedded (FFPE) tissue sections from ecDNA$^+$ ($n = 2$; VR01 and VR06) and ecDNA$^-$ ($n = 2$; VR23 and VR35) PDAC samples. We used the Xenium multi-tissue panel (377 genes) with 37 added-on genes to generate high-resolution expression data for a total of 414 genes (Supplementary Table 6). The added genes were carefully curated to capture the biological heterogeneity of PDAC cell states (Supplementary Table 6). Post-Xenium haematoxylin and eosin staining enabled cross-referencing of spatial transcriptomics data with morphological annotation by pathologists (A. Scarpa and C.L.; Extended Data Fig. 8a). Adjacent sections were used for FISH analysis

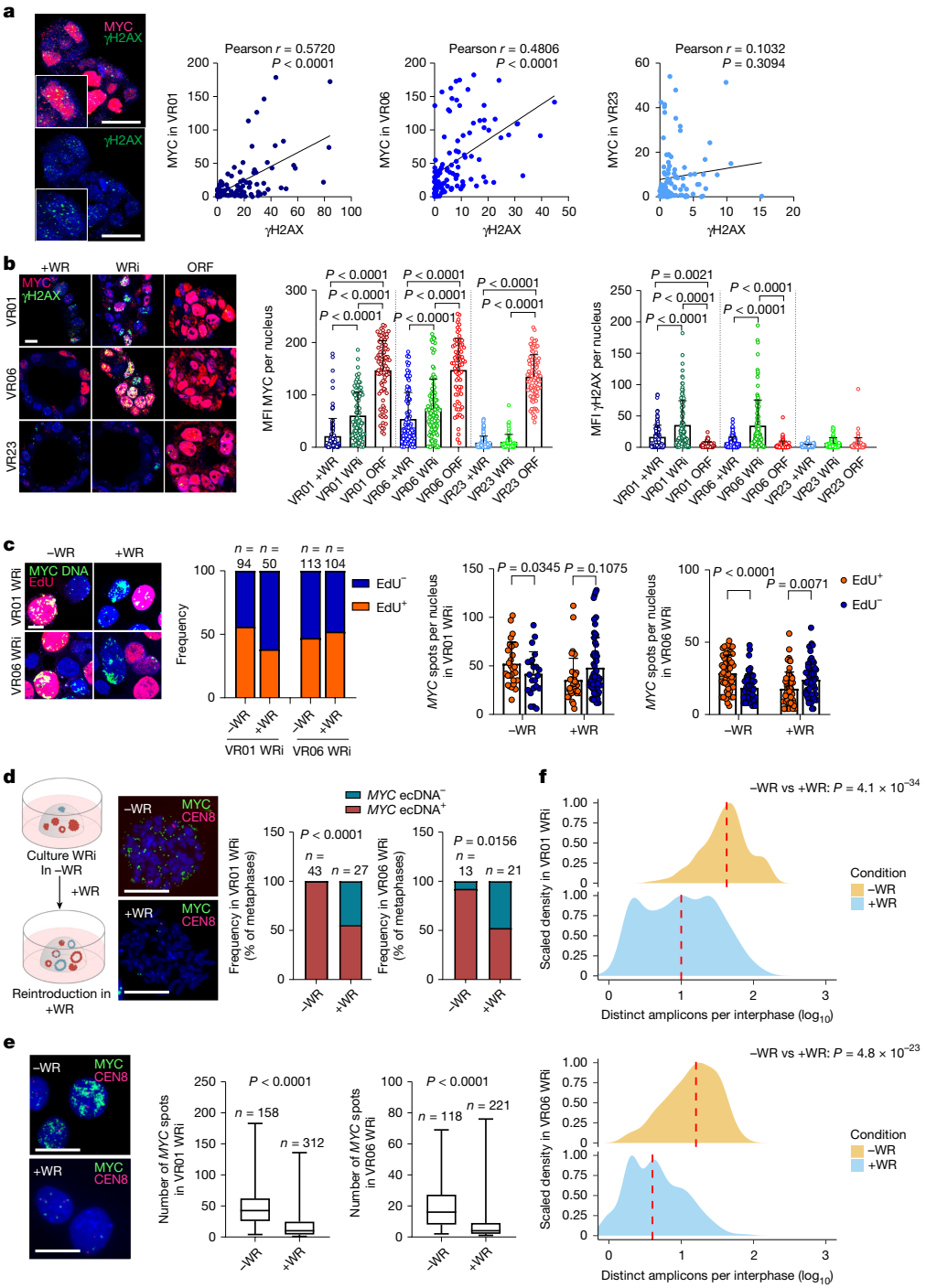

Fig. 4 | The fitness cost of an elevated ecDNA per cell content. a, Representative immunofluorescence for MYC and γH2AX in the ec*MYC* organoid at baseline (left). Scale bars, 20 µm. Per-cell MYC and γH2AX mean fluorescent intensity (MFI) in PDO cultures (two-sided Pearson's *r*; VR01 $n = 105$, VR06 $n = 107$ and VR23 $n = 99$) (right). **b**, Immunofluorescence for MYC and γH2AX in three conditions: +WR (baseline), WRi and ORF (exogenous MYC overexpression) (left). Scale bar, 10 µm. MYC and γH2AX expression per nucleus is also provided (middle and right, respectively). Data are mean ± s.d.; VR01 +WR $n = 105$, VR01 WRi $n = 98$, VR01 ORF $n = 84$, VR06 +WR $n = 107$, VR06 WRi $n = 101$, VR06 ORF $n = 74$, VR23 +WR $n = 99$, VR23 WRi $n = 71$ and VR23 ORF $n = 91$. The *P* values were determined by one-way analysis of variance with Tukey's multiple comparisons test. **c**, Immuno-FISH for *MYC* ecDNA and EdU in WRi PDOs cultivated ±WNT agonists for 3 days (left). Scale bar, 10 µm. Frequency of EdU⁺ and EdU⁻ nuclei in each condition (middle). *MYC* copies per nucleus stratified by EdU status (right). Data are mean ± s.d. The *P* values were determined by two-tailed Student's *t*-test. Quantifications from one experiment: VR01 WRi –WR $n = 94$, VR01 WRi +WR $n = 50$, VR06 WRi –WR $n = 113$ and VR06 WRi +WR $n = 104$. **d**, Schematic of the experiment (left). Representative FISH metaphase for VR01 WRi cultured in ±WR media for 30 days (middle). Scale bars, 20 µm. Frequency of *MYC* ecDNA⁺ metaphases (right): VR01 WRi –WR $n = 43$, VR01 WRi +WR $n = 27$, VR06 WRi –WR $n = 13$ and VR06 WRi +WR $n = 21$. The *P* values were determined by Fisher's exact two-sided test. The schematic in panel **d** was created in BioRender. Corbo, V. (2025) https://BioRender.com/f18c396. **e**, Representative FISH interphases for WRi VR01 in ±WR media for 30 days (left). Scale bars, 20 µm. *MYC* spots per nucleus quantified for VR01 and VR06 WRi cultures (right). The boxplots show the median (centre line), upper and lower quartiles (box limits), and 1.5× interquartile range (whiskers). VR01 WRi –WR $n = 158$ cells, VR01 WRi +WR $n = 312$ cells, VR06 WRi –WR $n = 118$ cells and VR06 WRi +WR $n = 221$ cells. The *P* values were determined by Wilcoxon rank-sum two-sided test. **f**, VR01 (top) and VR06 (bottom) shifted *MYC* ecDNA copy number distribution following the reintroduction of WNT agonists for 30 days. The *P* values were determined by Wilcoxon rank-sum two-sided test. The red dashed line indicates the median copy number state.

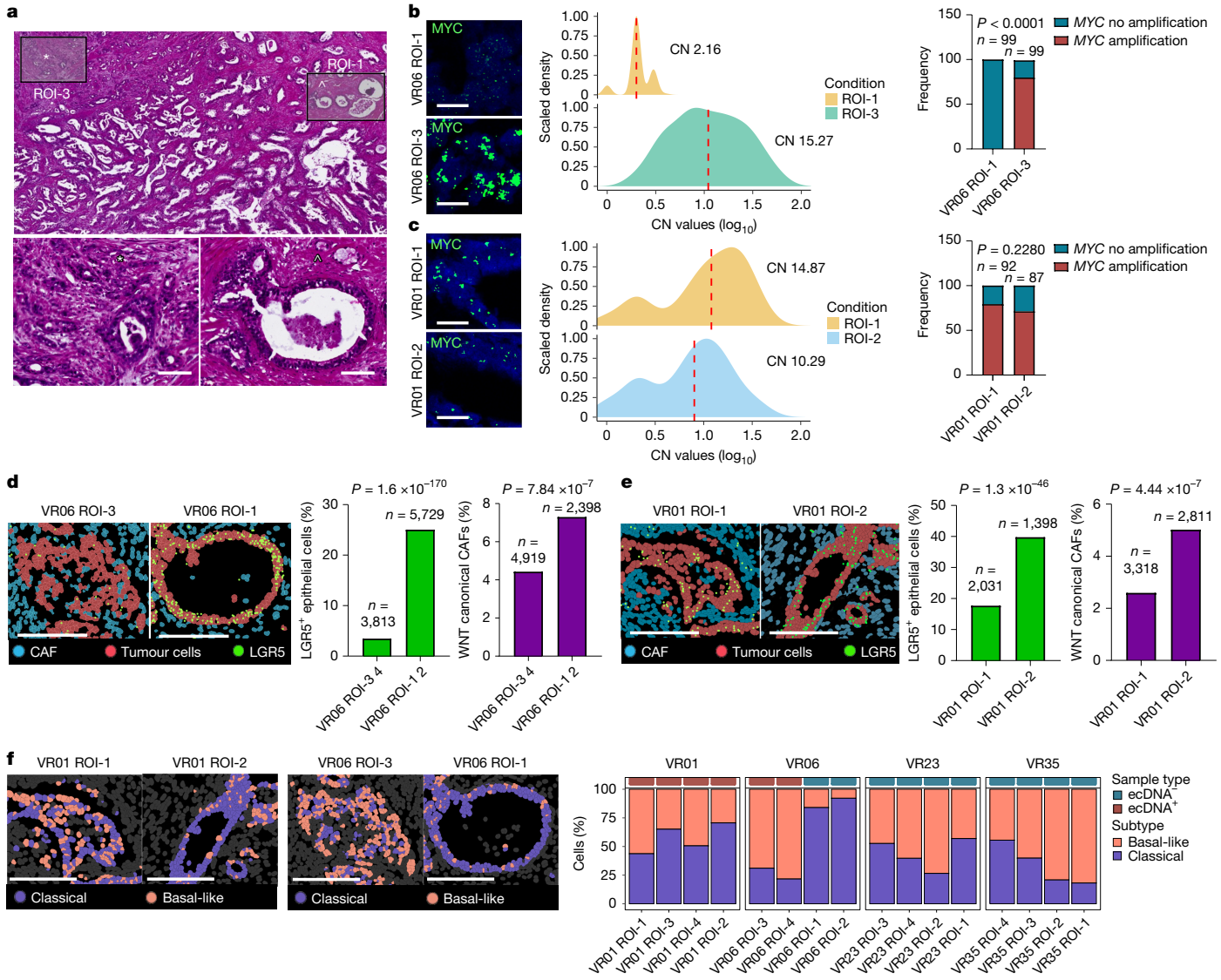

Fig. 5 | Spatial mapping of ecDNA-driven *MYC* amplifications and epithelial cell states. a, Post-Xenium haematoxylin and eosin of VR06-P (top). The magnifications of ROI-1 (caret; bottom right) and ROI-3 (asterisk; bottom left) demonstrate the different morphology of the neoplastic epithelium. Scale bars, 100 µm. **b**, Interphase FISH of ROI-1 and ROI-3 from VR06-P (left). Scale bars, 20 µm. Distribution of *MYC* copy number (CN) states per nucleus with indication of the average *MYC* copy number per ROI (middle). The dashed red line indicates the median copy number state. In the two selected ROIs, the proportion of nuclei (ROI-1 $n = 99$ and ROI-3 $n = 99$) with *MYC* amplification (defined as copy number > 5) is shown (right). The *P* value was calculated using Fisher's exact two-sided test. **c**, Interphase FISH of ROI-1 and ROI-2 from VR01-P (left). Scale bars, 20 µm. Distribution of *MYC* copy number states per nucleus with indication of the average *MYC* copy number per ROI (middle). The dashed red line indicates the median copy number state. In the two selected ROIs, the proportion of nuclei (ROI-1 $n = 92$ and ROI-2 $n = 87$) with *MYC* amplification (defined as copy number > 5) is also shown (right). The *P* value was calculated using Fisher's exact two-sided test. **d**,**e**, Xenium spatial plots showing localization of *LGR5* in the epithelial cells of the selected ROIs (left), and the frequency of epithelial cells expressing *LGR5* (middle) and cancer-associated fibroblasts (CAFs) expressing canonical WNT ligands (right) in the selected ROIs from VR06 (**d**) and VR01 (**e**). The *P* values were determined by a Chi-squared test (two-sided). Scale bars, 200 µm. **f**, Xenium spatial plot showing localization of neoplastic cells classified as either classical or basal-like (left). Scale bars, 200 µm. Distribution of individual epithelial subtypes within the indicated ROIs for each tissue (right). Areas presenting *MYC* amplification or not are annotated on top.

of *MYC*. Across all sections, 805,966 cells and 84,085,471 total transcripts (Q score ≥ 20) were analysed. Transcripts were assigned to cells as previously described[44]. Dimensionality reduction of the spatial transcriptomics data from the four tissues returned ten annotated clusters (Extended Data Fig. 8b), which we mapped to individual Xenium slides to generate spatial plots (Extended Data Fig. 8c). The mRNA-based annotation of tumour and stromal cells, as well as their spatial distribution, aligned with pathological annotations (Extended Data Fig. 8c). Next, we selected four regions of interest (ROIs) per tissue, ensuring that each was either morphologically distinct or surrounded by a unique microenvironment (Extended Data Fig. 8a).

We observed an extremely wide distribution of per cell copy number states and a high average *MYC* copy number in all four selected ROIs from VR01, as well as in two of the ROIs for VR06 (Extended Data Fig. 8d). ecDNA-negative tissues exhibited lower *MYC* copy numbers and less cell-to-cell variation (Extended Data Fig. 8d). *MYC* mRNA levels varied widely but were significantly higher in ROIs with *MYC* amplification (Extended Data Fig. 8d,e). Spatial heterogeneity was prominent in VR06, where *MYC*-amplified cells localized to solid areas with trabecular and single-cell growth patterns, contrasting the glandular morphology of non-amplified cells (Fig. 5a,b). The fraction of amplified cells in solid areas of VR06 was around 80% (Fig. 5b), and the distribution of ecDNA

states, as well as the average copy number, closely resembled those observed in WRi VR06-O cultures (Fig. 3g). In VR01, we found no spatial segregation between ecDNA$^+$ or ecDNA$^-$ areas. The selected VR01 ROIs displayed an elevated fraction of *MYC*-amplified cells (Fig. 5c), with ROI-1 displaying the highest average *MYC* copy number.

Next, we sought to establish the in vivo relationship between ecDNA-driven *MYC* amplification and canonical WNT dependency. As *LGR5* expression marks canonical WNT-responsive cell states[30,45], we observed significant downregulation of *LGR5* in our cultures following the acquisition of the WRi phenotype (Extended Data Fig. 4m). Therefore, we used *LGR5* expression as a marker for epithelial cells responsive to canonical WNT signalling. In VR06, ecDNA$^+$ tissue subdomains (ROI-3 and ROI-4) showed reduced frequencies of *LGR5*-expressing epithelial cells (Fig. 5d and Extended Data Fig. 9a), which corresponded with lower expression of WNT agonists in stromal cells (Fig. 5d and Extended Data Fig. 9b). Similarly, in VR01, a comparison between the two ROIs with the highest (ROI-1) and the lowest (ROI-2) average *MYC* copy number revealed significantly lower expression of *LGR5* and WNT ligands in the tissue subdomain with higher *MYC* amplification (Fig. 5e and Extended Data Fig. 9c,d). The Xenium platform also mapped the location of immune and stromal cells within the selected ROIs. The variability in the prevalence of cell types was greater between patients than within patients, except in VR06, where tumour areas with high *MYC* amplification showed an abundance of CAF-2 (CD90$^+$ myofibroblastic cancer-associated fibroblasts[46]; Extended Data Fig. 9e). Overall, cytotoxic T cells displayed reduced frequency in areas with high *MYC* amplification (Extended Data Fig. 9f). Across ROIs, PDAC cell states showed subtype mixing at the level of individual glands (Fig. 5f). Few ROIs presented a predominance of a singular subtype, such as basal-like cells in ecDNA$^+$ ROIs of VR06 (Fig. 5f).

Discussion

Intratumour heterogeneity and phenotypic plasticity drive tumour progression and therapy resistance. Oncogene dosage variation contributes to cell-state transition and phenotypic heterogeneity[1–3], thereby providing a substrate for somatic evolution. Nonetheless, the genetic mechanisms underlying phenotypic heterogeneity are still poorly understood. Although oncogene transcription can be driven by genetic or non-genetic mechanisms, focal amplifications are a key driver of oncogenic activation[47]. ecDNAs are emerging as important mediators of intratumour heterogeneity and therapy resistance in cancer[6]. Thousands of ecDNA copies may accumulate in a cancer cell and accordingly increase oncogene expression. However, it remains debated whether transcriptional output from ecDNA is solely a reflection of copy number or influenced by ecDNA clustering and colocalization with transcriptional hubs[24,28,48].

In PDAC, amplifications of oncogenes, such as *GATA6*, *KRAS* and *MYC*, shape tumour evolution[3,49]. Sustained *MYC* activity is required for maintenance and progression of PDAC[15,16,50]. Amplifications of *MYC* are specifically enriched in metastatic PDAC[15,16], highlighting the need to understand the genetic drivers of *MYC* heterogeneity.

Here we provide a detailed analysis of ecDNAs in PDAC. We have demonstrated that ecDNAs are a major source of high-level amplifications in key PDAC oncogenes and a major contributor to *MYC* heterogeneity in PDAC. PDOs and tissues harbouring *MYC* on ecDNA displayed significant heterogeneity of *MYC* copy number and expression, compared with tumours having *MYC* on chromosomal DNA. Nonetheless, the transcriptional output from ecDNA was not solely dependent on copy number but modulated by the presence or absence of *cis*-regulatory elements, such as the *PVT1* promoter. Although we observed evidence for ecDNA clustering and their JQ1-induced dispersal, as reported by Hung and colleagues for ec*MYC*-bearing cell lines[28], *MYC* expression was not necessarily amplified from ecDNA. This underscores the importance of the regulatory landscape of ecDNA in controlling gene expression.

Our data suggest that p53 inactivation is a prerequisite for ecDNA formation in PDAC. All tumours harbouring ecDNA exhibited biallelic p53 disruption but did not always show evidence of extensive genomic instability, such as chromothripsis or whole-genome duplication. Therefore, ecDNA formation in PDAC may occur through mechanisms distinct from catastrophic genomic events, potentially during later stages of tumour evolution when selective pressures intensify. However, detailed analysis of precancerous and cancerous lesions is essential to determine whether ecDNA formation arises early in tumorigenesis or later as a consequence of genomic instability.

Our analysis revealed that *MYC* amplification on ecDNA provides a deterministic mechanism for rapid environmental adaptation. A WNT-depleted culture environment drove the rapid selection of cells carrying from dozens to hundreds of ecDNA molecules that could proliferate independently of stromal signals. The removal of the selective pressure reversed this process, leading to a large population of cells carrying fewer copies of ecDNAs and accordingly reduced *MYC* expression.

An elevated burden of ecDNAs imposes a fitness cost on cancer cells. The accumulation of hundreds of ecDNAs per cell, but not oncogene levels per se, was associated with abundant γH2AX foci and reduced proliferation. Our result suggests that the large number of ecDNA might not be tolerated unless providing enhanced fitness in specific microenvironmental conditions.

Our data further indicate that elevated *MYC* activity is critical for PDAC cells to achieve stromal independence, particularly regarding WNT signalling. ecDNA-driven *MYC* amplification induced predictable transcriptomic changes and shifted morphology towards solid growth patterns, which were reversible upon withdrawal of selective pressure. Although ecDNA accumulation intensified cancer cell reliance on *MYC* transcription, it did not necessarily induce a full transition towards a squamous phenotype. The integration of cellular and spatial profiles of human tissues revealed that ecDNA *MYC* amplifications are associated with non-responsive WNT states and morphologies shifting from glandular to solid structures.

Collectively, our work establishes *MYC* ecDNAs as a key driver of genomic plasticity in PDAC, where they promote rapid and flexible adaptation by amplifying oncogenes, creating heterogeneity and enabling reversible phenotypic changes.

Online content

Any methods, additional references, Nature Portfolio reporting summaries, source data, extended data, supplementary information, acknowledgements, peer review information; details of author contributions and competing interests; and statements of data and code availability are available at https://doi.org/10.1038/s41586-025-08721-9.

1. Bielski, C. M. et al. Widespread selection for oncogenic mutant allele imbalance in cancer. *Cancer Cell* **34**, 852–862.e4 (2018).
2. Marusyk, A., Janiszewska, M. & Polyak, K. Intratumor heterogeneity: the Rosetta stone of therapy resistance. *Cancer Cell* **37**, 471–484 (2020).
3. Mueller, S. et al. Evolutionary routes and KRAS dosage define pancreatic cancer phenotypes. *Nature* **554**, 62–68 (2018).
4. Yi, E. et al. Live-cell imaging shows uneven segregation of extrachromosomal DNA elements and transcriptionally active extrachromosomal DNA hubs in cancer. *Cancer Discov.* **12**, 468–483 (2022).
5. Levan, G., Mandahl, N., Bregula, U., Klein, G. & Levan, A. Double minute chromosomes are not centromeric regions of the host chromosomes. *Hereditas* **83**, 83–90 (1976).
6. Lange, J. T. et al. The evolutionary dynamics of extrachromosomal DNA in human cancers. *Nat. Genet.* **54**, 1527–1533 (2022).
7. Haber, D. A. & Schimke, R. T. Unstable amplification of an altered dihydrofolate reductase gene associated with double-minute chromosomes. *Cell* **26**, 355–362 (1981).
8. Nathanson, D. A. et al. Targeted therapy resistance mediated by dynamic regulation of extrachromosomal mutant EGFR DNA. *Science* **343**, 72–76 (2014).
9. Schulte, A. et al. Glioblastoma stem-like cell lines with either maintenance or loss of high-level EGFR amplification, generated via modulation of ligand concentration. *Clin. Cancer Res.* **18**, 1901–1913 (2012).
10. Bailey, P. et al. Genomic analyses identify molecular subtypes of pancreatic cancer. *Nature* **531**, 47–52 (2016).

11. Chan-Seng-Yue, M. et al. Transcription phenotypes of pancreatic cancer are driven by genomic events during tumor evolution. *Nat. Genet.* **52**, 231–240 (2020).
12. Martinelli, P. et al. GATA6 regulates EMT and tumour dissemination, and is a marker of response to adjuvant chemotherapy in pancreatic cancer. *Gut* **66**, 1665–1676 (2017).
13. Miyabayashi, K. et al. Intraductal transplantation models of human pancreatic ductal adenocarcinoma reveal progressive transition of molecular subtypes. *Cancer Discov.* **10**, 1566–1589 (2020).
14. Notta, F. et al. A renewed model of pancreatic cancer evolution based on genomic rearrangement patterns. *Nature* **538**, 378–382 (2016).
15. Hayashi, A. et al. A unifying paradigm for transcriptional heterogeneity and squamous features in pancreatic ductal adenocarcinoma. *Nat. Cancer* **1**, 59–74 (2020).
16. Maddipati, R. et al. MYC levels regulate metastatic heterogeneity in pancreatic adenocarcinoma. *Cancer Discov.* **12**, 542–561 (2022).
17. Boj, S. F. et al. Organoid models of human and mouse ductal pancreatic cancer. *Cell* **160**, 324–338 (2015).
18. Driehuis, E. et al. Pancreatic cancer organoids recapitulate disease and allow personalized drug screening. *Proc. Natl Acad. Sci. USA* **116**, 26580–26590 (2019).
19. Tiriac, H. et al. Organoid profiling identifies common responders to chemotherapy in pancreatic cancer. *Cancer Discov.* **8**, 1112–1129 (2018).
20. Deshpande, V. et al. Exploring the landscape of focal amplifications in cancer using AmpliconArchitect. *Nat. Commun.* **10**, 392 (2019).
21. Kim, H. et al. Extrachromosomal DNA is associated with oncogene amplification and poor outcome across multiple cancers. *Nat. Genet.* **52**, 891–897 (2020).
22. Tsai, S. Q. et al. CIRCLE-seq: a highly sensitive in vitro screen for genome-wide CRISPR–Cas9 nuclease off-targets. *Nat. Methods* **14**, 607–614 (2017).
23. Turner, K. M. et al. Extrachromosomal oncogene amplification drives tumour evolution and genetic heterogeneity. *Nature* **543**, 122–125 (2017).
24. Wu, S. et al. Circular ecDNA promotes accessible chromatin and high oncogene expression. *Nature* **575**, 699–703 (2019).
25. Drews, R. M. et al. A pan-cancer compendium of chromosomal instability. *Nature* **606**, 976–983 (2022).
26. Takahashi, N. et al. Replication stress defines distinct molecular subtypes across cancers. *Cancer Res. Commun.* **2**, 503–517 (2022).
27. Carter, S. L., Eklund, A. C., Kohane, I. S., Harris, L. N. & Szallasi, Z. A signature of chromosomal instability inferred from gene expression profiles predicts clinical outcome in multiple human cancers. *Nat. Genet.* **38**, 1043–1048 (2006).
28. Hung, K. L. et al. ecDNA hubs drive cooperative intermolecular oncogene expression. *Nature* **600**, 731–736 (2021).
29. Cho, S. W. et al. Promoter of lncRNA gene PVT1 is a tumor-suppressor DNA boundary element. *Cell* **173**, 1398–1412.e22 (2018).
30. Tamagawa, H. et al. Wnt-deficient and hypoxic environment orchestrates squamous reprogramming of human pancreatic ductal adenocarcinoma. *Nat. Cell Biol.* https://doi.org/10.1038/s41556-024-01498-5 (2024).
31. Seino, T. et al. Human pancreatic tumor organoids reveal loss of stem cell niche factor dependence during disease progression. *Cell Stem Cell* **22**, 454–467.e6 (2018).
32. He, T. C. et al. Identification of c-MYC as a target of the APC pathway. *Science* **281**, 1509–1512 (1998).
33. Acar, A. et al. Exploiting evolutionary steering to induce collateral drug sensitivity in cancer. *Nat. Commun.* **11**, 1923 (2020).
34. Turinetto, V. & Giachino, C. Multiple facets of histone variant H2AX: a DNA double-strand-break marker with several biological functions. *Nucleic Acids Res.* **43**, 2489–2498 (2015).
35. Raymond, E. et al. Effects of hydroxyurea on extrachromosomal DNA in patients with advanced ovarian carcinomas. *Clin. Cancer Res.* **7**, 1171–1180 (2001).
36. Schoenlein, P. V. et al. Radiation therapy depletes extrachromosomally amplified drug resistance genes and oncogenes from tumor cells via micronuclear capture of episomes and double minute chromosomes. *Int. J. Radiat. Oncol. Biol. Phys.* **55**, 1051–1065 (2003).
37. Von Hoff, D. D. et al. Hydroxyurea accelerates loss of extrachromosomally amplified genes from tumor cells. *Cancer Res.* **51**, 6273–6279 (1991).
38. Carroll, S. M. et al. Double minute chromosomes can be produced from precursors derived from a chromosomal deletion. *Mol. Cell. Biol.* **8**, 1525–1533 (1988).
39. Ruiz, J. C. & Wahl, G. M. Chromosomal destabilization during gene amplification. *Mol. Cell. Biol.* **10**, 3056–3066 (1990).
40. Moffitt, R. A. et al. Virtual microdissection identifies distinct tumor- and stroma-specific subtypes of pancreatic ductal adenocarcinoma. *Nat. Genet.* **47**, 1168–1178 (2015).
41. Raghavan, S. et al. Microenvironment drives cell state, plasticity, and drug response in pancreatic cancer. *Cell* **184**, 6119–6137.e26 (2021).
42. Zhu, Y. et al. Oncogenic extrachromosomal DNA functions as mobile enhancers to globally amplify chromosomal transcription. *Cancer Cell* **39**, 694–707.e7 (2021).
43. Delmore, J. E. et al. BET bromodomain inhibition as a therapeutic strategy to target c-Myc. *Cell* **146**, 904–917 (2011).
44. Janesick, A. et al. High resolution mapping of the tumor microenvironment using integrated single-cell, spatial and in situ analysis. *Nat. Commun.* **14**, 8353 (2023).
45. Torborg, S. R. et al. Solid tumor growth depends on an intricate equilibrium of malignant cell states. Preprint at *bioRxiv* https://doi.org/10.1101/2023.12.30.573100 (2023).
46. Elyada, E. et al. Cross-species single-cell analysis of pancreatic ductal adenocarcinoma reveals antigen-presenting cancer-associated fibroblasts. *Cancer Discov.* **9**, 1102–1123 (2019).
47. Beroukhim, R. et al. The landscape of somatic copy-number alteration across human cancers. *Nature* **463**, 899–905 (2010).
48. Purshouse, K. et al. Oncogene expression from extrachromosomal DNA is driven by copy number amplification and does not require spatial clustering in glioblastoma stem cells. *eLife* https://doi.org/10.7554/eLife.80207 (2022).
49. Baslan, T. et al. Ordered and deterministic cancer genome evolution after p53 loss. *Nature* **608**, 795–802 (2022).
50. Sodir, N. M. et al. MYC instructs and maintains pancreatic adenocarcinoma phenotype. *Cancer Discov.* **10**, 588–607 (2020).

Methods

Human specimens and clinical data

PDAC tissues were obtained from the General and Pancreatic Surgery Unit at the University of Verona. Written informed consent was obtained from patients preceding the acquisition of the specimens. The fresh tissues used to establish PDOs and associated clinical and follow-up data were collected under a study approved by the Integrated University Hospital Trust (AOUI) Ethics Committee (Comitato Etico Azienda Ospedaliera Universitaria Integrata): approval number 1911 (protocol number 61413, Prog 1911 on 19 September 2018). FFPE tissues were collected under protocol number 1885 approved by the AOUI Ethics Committee and retrieved from the ARC-NET Biobank.

PDO establishment and culture

PDAC PDOs were established following previously published procedures[17]. The specimens used to generate PDOs were examined by pathologists to confirm the presence of neoplastic cells. In brief, tissue specimens were minced and digested with collagenase II (5 mg ml^{-1}; Gibco) and dispase I (1.25 mg ml^{-1}; Gibco) in human splitting medium (HSM; advanced Dulbecco's modified eagles medium with nutrient mixture F-12 Hams (Gibco) supplemented with HEPES (10 mM; Gibco), Glutamax (2 mM; Gibco) and Primocin (1 mg ml^{-1}; InvivoGen)) at 37 °C for a maximum of 2 h, followed by an additional 15-min digestion with TrypLE (Gibco) at 37 °C. The digested material was embedded in growth factor-reduced Matrigel (Corning) and overlaid with human complete medium (+WR; mouse epidermal growth factor (50 ng ml^{-1}; Gibco), B-27 Supplement (1X; Gibco), nicotinamide (10 mM; Sigma-Aldrich), *N*-acetylcysteine (1.25 mM; Sigma-Aldrich), FGF10 (100 ng ml^{-1}; Peprotech), Y-27632 dihydrochloride (10.5 µM; Sigma), gastrin (10 nM; Tocris), TGFβ receptor inhibitor A83-01 (500 nM; Tocris), WNT3A-conditioned media (50% v/v), RSPO1-conditioned media (10% v/v) and mouse Noggin (100 ng ml^{-1}; Peprotech)). Media were refreshed every 3–4 days. For organoid propagation, confluent organoids were removed from Matrigel, dissociated into small clusters of cells by pipetting, and resuspended in an appropriate volume of fresh Matrigel. All organoid models were acquired as part of the HCMI (https://ocg.cancer.gov/programs/HCMI) and are available for access from the American Type Culture Collection (ATCC). For each PDO, Supplementary Table 1 provides two unique identifiers (study ID and HCMI ID), along with the clinical and follow-up data associated with the corresponding case. The HCMI ID can be queried in the HCMI searchable catalogue (https://hcmi-searchable-catalog.nci.nih.gov/). Dependency of organoid cultures to WNT3A and RSPO1 was assessed on nine PDOs (VR01, VR02, VR06, VR09, VR20, VR21, VR23, VR29 and VR32). Organoid cultures were passaged once a week with a splitting ratio of 1:3 in +WR or human-depleted media (−WR; mouse epidermal growth factor (50 ng ml^{-1}; Gibco), B-27 supplement (1X; Gibco), nicotinamide (10 mM; Sigma-Aldrich), *N*-acetylcysteine (1.25 mM; Sigma-Aldrich), FGF10 (100 ng ml^{-1}; Peprotech), and gastrin (10 nM; Tocris)). To establish WRi PDOs, organoids established and propagated in +WR were placed and maintained in −WR until the emergence of WRi. Owing to the cell death induced by −WR, the media were refreshed every 3 days and Matrigel every 14 days without propagating the cultures, until the emergence of WRi PDOs. The growth curve of WRi PDOs was obtained by plotting the number of domes (one dome refers to 50 µl of Matrigel) at different days of culture in −WR. WRi PDOs were reintroduced in +WR or maintained in −WR (control) for five passages before collection of metaphase spreads and proteins. To obtain 'late-passage' PDOs, organoids were passaged 40 times post-establishment in +WR medium. For the Wnt-C59 experiment, baseline and adapted organoids were passaged every 7 days with a splitting ratio of 1:3 in the presence of Wnt-C59 (100 nM; Selleckchem). Wnt-C59 was added to the culture at the day of splitting and after 3 days of culture. Organoids were routinely tested for the presence of *Mycoplasma* contamination using the Mycoalert Mycoplasma Detection kit (Lonza).

Single-cell dissociation from organoids

Organoids were incubated with dispase I diluted in HSM (2 mg ml^{-1}; dispase I solution) for 20 min at 37 °C to digest Matrigel. Following this, organoids were dissociated using TrypLE (Gibco) for 10 min at 37 °C, incubated in dispase I solution for additional 10 min at 37 °C, and pipetted to obtain single-cell suspension.

Assessing *MYC* activation by WR media

PDOs were dissociated into single cells as previously described and plated in Matrigel in +WR (100,000 viable cells per condition). Following organoid reformation in +WR, PDOs were starved overnight in HSM. Post-starvation, PDOs were stimulated with +WR, −WR or HSM for 8 h, before collection and isolation of RNA.

JQ1 in vitro treatment

Organoids were dissociated into single cells as previously described. One thousand viable cells were plated in 100 µl 10% Matrigel/media per well in a 96-well plate in triplicates. JQ1 (500 nM; S7110, Selleckchem) or vehicle was added 40 h after plating once the organoids were reformed. After 72 h of treatment, cell viability was assessed using CellTiter-Glo (Promega) following the manufacturer's instructions. Results were normalized to the vehicle control of each PDO. In parallel, 20,000 viable cells per 50 µl Matrigel were plated and supplemented with media. Following organoid reformation, cells were treated with JQ1 (500 nM) or vehicle control, and RNA, and metaphase spreads were collected after 72 h.

Lentiviral production and infection of organoids

To overexpress *MYC*, we used a lentiviral vector carrying an open-reading frame for *MYC* (mGFP tagged; RC201611L4, Origene). Lentivirus was produced by transfecting the plasmid containing *MYC*, and the packaging plasmid VSV-G with X-tremeGENE9 (6365779001, Roche Sigma-Aldrich) in HEK293T cells. The viral supernatant was harvested 48 h post-transfection and quantified using the Lenti-XTM qRT–PCR Titration kit (Takara Bio) according to the manufacturer's instructions. pLenti-C-MYC-DDK-P2A-Puro lentiORF control particles (PS100092V, Origene) were used as non-targeting control. The lentiviral barcoding library was produced by transfecting the plasmid library and the packaging plasmids pMD2.G and psPAX2 (gifts from D. Trono; Addgene plasmid #12259 and Addgene plasmid #12260) in HEK293T/17 cells (ATCC: CRL-11268). The viral supernatant was harvested 48 h post-transfection and concentrated with Lenti-X Concentrator (Clontech), according to the manufacturer's instructions. Viral particles were resuspended in OPTI-MEM (Life Technologies), titrated using a fluorometric assay and stored at −80 °C. For infection, organoids were dissociated into single cells, resuspended in infection media (DMEM; Gibco), 5% fetal bovine serum (FBS; Gibco) and 1% penicillin–streptomycin (Gibco), supplemented with 1 µg ml^{-1} polybrene and lentiviral particles. Cells were then spinoculated for 1 h at room temperature and incubated at 37 °C for 16 h. Infected cells were then collected, embedded in Matrigel and overlayed with +WR media. Antibiotic selection was started 48 h after infection using 2 µg ml^{-1} puromycin (Gibco).

Barcoding of organoids

For barcoding experiment, we used a 1M-barcode pool from the CloneTracker XP 3M Barcode-3′ Library in pScribe4-RFP-Puro (Cellecta) kit. We infected 5×10^5 cells with 0.1 multiplicity of infection of virus to obtain a population of cells with a single barcode per cell. After infection, organoids were subjected to antibiotic selection using 2 µg ml^{-1} of puromycin (Gibco). Barcoded organoids were then divided into two conditions: +WR (control) and −WR (selective pressure) with at least two replicates per condition. An aliquot of barcoded organoids was collected for DNA extraction (P0). The control condition was expanded for five passages before collection of the pellet, whereas pellets from

the replicates in the presence of selective pressure were collected at the time of emergence of WR independence.

Organoid metaphase spreads and interphase nuclei

Organoids were incubated with Colcemid (1 μg ml^{-1}; Gibco) in culture media at 37 °C and 5% CO_2 overnight. Following incubation, organoids were dissociated into single cells as previously described. Single cells were incubated in hypotonic solution (potassium chloride 0.56% and sodium citrate 0.8%) for 20 min at room temperature. Nuclei were then fixed in ice-cold methanol–acetic acid (3:1), washed with methanol–acetic acid (2:1) and dropped on adhesion microscope slides.

DNA FISH

DNA FISH was performed using the ZytoLight SPEC MYC/CEN8 Dual Color FISH probe (ZytoVision). Before hybridization, tissues were deparaffinized and rehydrated, pre-treated with 0.1 citrate buffer (pH 6) solution at 85 °C for 30 min, followed by pepsin treatment (4 mg ml^{-1} in 0.9% NaCl, pH 1.5) for 4 min at 37 °C. For both tissues and PDOs, the probes were applied to the slides and sealed with rubber cement and incubated in a humidified atmosphere (Thermobrite System) at 80 °C for 10 min to allow denaturation of the probes and of the DNA target. Slides were then incubated overnight at 37 °C to allow for hybridization. The rubber cement and the coverslip were then removed, and the slides were washed in 2X SSC/0.3 % NP-40 for 15 min at room temperature and then at 72 °C for 2 min. Following post-hybridization washes, slides were counterstained with DAPI 1 μg ml^{-1} (Kreatech, Leica). For tissues and embedded organoids, images were acquired on a FV4000 confocal microscope (Olympus Life Science). Nuclei were acquired and visualized in blue (DAPI). For PDOs, images were acquired with Leica TCS SP5 Fluorescent microscopes. The number of fluorescent signals for each probe for each nucleus, for both tissues and PDOs, was quantified with FIJI (ImageJ2 v2.9.0/1.53t) using the Find plugin maxima function in a supervised manner as previously described[6]. Interphase ecDNA clustering was quantified by the autocorrelation function as described in Hung et al.[28].

Histology and immunostaining

For histopathological analysis, organoids were released from Matrigel using dispase I solution as previously described, fixed with 10% neutral-buffered formalin for 20 min, and embedded in Histogel processing gel (Fisher Scientific). Histogel-embedded organoids were processed according to routine histology procedures and embedded in paraffin. To account for the effect of the media, +WR PDOs were put in −WR for 24 h before embedding and fixation. Haematoxylin and eosin (H&E) staining and immunostainings were performed on sections of FFPE tissues and organoids, following established procedures using the reported primary antibodies: MYC (clone EP121, ALI415G7, Biocare for immunohistochemistry (IHC); clone Y69, ab32072, Abcam for immunofluorescence, dilution 1:500), GATA6 (polyclonal; AF1700, R&D Systems for IHC, dilution 1:200), ΔNp63 (clone BC28, PA0163, Leica for IHC), CK5 (clone XM26, PA0468, Novocastra for IHC, dilution 1:100) and γH2AX (clone CR55T33, 14-9865-82, eBioscience for immunofluorescence, dilution 1:500). For immunofluorescence, we used the following secondary antibody: Alexa Fluor 488 donkey anti-mouse (A21202, lot 1423052, Invitrogen, dilution 1:500), Alexa Fluor Plus555 goat anti-rabbit (A32732, lot VC297826, Invitrogen, dilution 1:500). Immunohistochemistry slides were then scanned and digitalized using the Aperio Scan-Scope XT Slide Scanner (Aperio Technologies). In tissues, quantification of MYC staining was performed on 20 areas for each tissue and reported as the *H*-score. In organoids, MYC and GATA6 staining was quantified as the percentage of positive nuclei per organoid, using Aperio ImageScope. For immunofluorescence, images were acquired by the FV4000 confocal microscope (Olympus Life Science) and quantified using ImageJ (https://imagej.nih.gov/).

ImmunoFISH

Single-cell suspension from baseline PDOs was obtained as previously described, then spun at 1,000 rpm for 5 min on slides using the Cytospin 4 cytocentrifuge and fixed by 4% paraformaldehyde (PFA) for 15 min. After washing in PBS, cells were permeabilized with 0.4% Triton for 10 min and incubated for 1 h in blocking solution (5% BSA, 5% goat serum and 0.1% Triton). After incubation with primary (MYC; ab32072, Abcam, dilution 1:500) and secondary (Alexa Fluor 647 goat anti-rabbit; A-21245, lot 2833435, Invitrogen, dilution 1:500) antibodies, cells were fixed again with 4% PFA for 10 min and washed with 2X SSC buffer. The ZytoLight SPEC MYC/CEN8 Dual Color FISH probe (ZytoVision) was applied as previously described. Images were acquired with a FV4000 confocal microscope (Olympus Life Science) and quantified using ImageJ (https://imagej.nih.gov/).

Pulse EdU staining

Baseline and WRi organoids were cultured for 3 days in +WR and −WR. At day 3, fresh media with EdU (10 μM) was added for 1 h before organoid collection and dissociation into single-cell suspension. Cells were spun on slides, fixed with 4% PFA and washed with 3% BSA in PBS. EdU detection was performed following the manufacturer's instructions (Click-iT EdU imaging kit Alexa Fluor 555, C10338, Invitrogen), followed by a second fixation with 4% PFA for 10 min. FISH was performed as previously described using the ZytoLight SPEC MYC/CEN8 Dual Color FISH probe (ZytoVision). Images were acquired with a FV4000 confocal microscope (Olympus Life Science) and quantified using ImageJ (https://imagej.nih.gov/).

RNAScope

MYC mRNA in situ detection on embedded organoids was performed using the RNAScope Multiplex Fluorescent Reagent kit v2 (323100, Bio-Techne) following the manufacturer's instructions. The target probe Hs-MYC-C2 (311761-C2, Bio-Techne) together with the Opal 570 fluorophores were used. The nuclei were counterstained and visualized using DAPI fluorescent dye. Images were acquired with a FV4000 confocal microscope (Olympus Life Science) and quantified using ImageJ (https://imagej.nih.gov/).

Immunoblotting

Proteins were prepared using cell lysis buffer (Cell Signaling Technology) supplemented with protease inhibitor cocktail (Sigma) and the phosphatase inhibitor PhosphoSTOP (Roche). Protein lysates were separated on 4–12% Bis-Tris NuPAGE gels (Life technologies), transferred to a PDVF membrane (Millipore) and then incubated with the reported antibodies: MYC (clone Y69, ab32072, lot 1012026-1, Abcam, dilution 1:1,000), γH2AX (clone EP854(2)Y, ab81299, lot GR3203642-4, Abcam, dilution 1:1,000), GFP (clone D5.1, 2956, lot 6, Cell Signaling Technologies, dilution 1:1,000), GAPDH (clone D16H11, 5174, lot 6, Cell Signaling Technologies, dilution 1:5,000) and histone H3 (polyclonal, 09-838, lot 2698469, Sigma-Aldrich, dilution 1:5,000) primary antibodies, and the peroxidase-conjugated AffiniPure donkey anti-rabbit (polyclonal, 711-035-152, Jackson Immunoresearch Laboratories) secondary antibody. To account for the effect of the media, +WR PDOs were put in −WR for 24 h before collection of the pellet of the cells. For gel source data, see Supplementary Fig. 1.

Quantitative real-time PCR analysis

RNA from organoids were isolated using the TRIzol reagent (Life Technologies), followed by the column-based PureLink RNA Mini Kit (Thermo Fisher Scientific). Reverse transcription of 1 μg of RNA was performed using the TaqMan Reverse Transcription reagents (Applied Biosystems), and 20 ng of cDNA was used in the PCR. The following TaqMan probes *HPRT1* (Hs02800695_m1) and *LGR5* (Hs00173664_m1) were used. The following primers (Eurofins) were used with SYBR Green

PCR master mix (Thermo Fisher): *MYC* forward: CCTGGTGCTCCATGAGGAGAG; *MYC* reverse: CAGACTCTGACCTTTTGCCAG; *GAPDH* forward: ACAGTTGCCATGTAGACC; *GAPDH* reverse: TTTTTGGTTGAGCACAGG.

Relative gene expression quantification was performed using the ΔΔCt method with the Sequence Detection Systems Software, v1.9.1 (Applied Biosystems).

DNA isolation

Organoids were incubated in Cell Recovery Solution (Corning) for 30 min at 4 °C to remove Matrigel, and were pelleted by centrifuging at 10,000*g* for 5 min at 4 °C. For tissues, slices from snap-frozen PDAC tissues were assessed by a pathologist for percent neoplastic cellularity, and only tissues with higher than 20% neoplastic cellularity were used. For WGS and panel DNA sequencing, DNA isolation was performed using the DNeasy Blood & Tissue kit (Qiagen). For CIRCLE-seq, high-molecular-weight DNA was extracted using the MagAttract HMW DNA Kit (Qiagen).

Whole-genome sequencing

DNA quality was assessed by DNF-467 genomic DNA 50 kb Kit on a Bioanalyzer 2100 (Agilent). Libraries were prepared and sequenced using NovaSeq 6000 S4 Reagent Kit v1.5 (300 cycles) at 15× coverage for 160 million reads per sample.

Data pre-processing and alignment. Sequencing data were pre-processed and mapped to the reference genome using the nf-core/sarek pipeline (v3.0.2)[51]. In brief, Fastp (v0.23.2)[52] removed low-quality bases and adapters, BWA Mem (v0.7.17-r1188)[53] mapped trimmed reads to the reference genome GRCh38 (v1.4.4), provided by the Genome Reference Consortium (https://www.ncbi.nlm.nih.gov/grc), mapped reads were marked for duplicates using Picard Markduplicates (v4.2.6.1), and read base-quality scores were recalibrated using GATK BaseRecalibrator (v4.2.6.1) and GATK ApplyBQSR (v4.2.6.1)[54].

Amplicon characterization. The nf-core/circdna (v1.0.1; https://github.com/nf-core/circdna) pipeline branch 'AmpliconArchitect' was used to define amplicon classes in each WGS sample. Nf-core/circdna calls copy number using cnvkit (v0.9.9)[55] and prepares amplified segments with a copy number greater than 4.5 for AmpliconArchitect by utilizing the functionality of the AmpliconSuite-Pipeline (https://github.com/jluebeck/AmpliconSuite-pipeline). AmpliconArchitect (v1.3_r1)[20] was ran on the aligned reads and the amplified seeds to delineate the amplicon structures. Identified amplicons were then classified using AmpliconClassifier (v0.4.11)[56] into circular (ecDNA), linear (linear amplicon), complex (complex amplicon) or BFB (amplicon with a breakage-fusion-bridge signature). Samples containing at least one circular amplicon (ecDNA) were termed 'ecDNA$^+$', whereas samples without ecDNA amplicons were termed 'ecDNA$^-$'. Samples were also classified into 'circular', 'linear', 'complex', 'BFB' or 'no-fSCNA' (no-focal somatic copy number amplification detected) by the types of amplicons they contained (see Kim et al.[21]). Samples with multiple amplicons were classified based on the amplicon with the highest priority. The priority is: circular > BFB > complex > linear. The amplicon similarity score and its *P* values were calculated based on the amplicon regions and breakpoint overlap as described in Luebeck et al.[56].

Copy number calling. Copy number calls of the WGS samples were generated by cnvkit (v0.9.9)[55]. The identified segments were then classified as gain (copy number ≥ 3), loss (copy number ≤ 1) or deep loss (copy number ≤ 0.25).

Chromosomal instability signatures. Chromosomal instability signatures, including the CX9 replication stress signature, were assessed from the WGS copy number profiles using the R-package CINSignatureQuantification[25].

Ploidy analysis. Sample ploidy was derived using PURPLE (v3.8.1)[57], which estimates copy number and ploidy by using read depth ratio and tumour B allele frequency from COBALT (v3.9) and AMBER (v1.14), respectively (https://github.com/hartwigmedical/hmftools). COBALT, AMBER and PURPLE were used in tumour-only mode using their default parameters. Of note, PURPLE was used with a fixed parameter value of purity set to 1 for all samples, ensuring consistency in the analysis.

CIRCLE-seq

To enrich circular DNA for sequencing, each DNA sample was digested for 7 consecutive days with ATP-dependent Plasmid-Safe DNase (Lucigen) to remove linear/chromosomal DNA. Each day, 20 units of enzyme and 4 µl of a 25 mM ATP solution were added. After 7 days, the DNase was heat-inactivated for 30 min at 70 °C. The fold-change reduction in linear DNA was assessed by qPCR targeting the chromosomal gene *HBB* and the mitochondrial gene *MT-CO1*. Amplification of circular DNA was performed with a Phi29 polymerase as described in Koche et al.[58]. Amplified circular DNAs were then prepared for sequencing. In brief, around 550 ng of DNA was sheared to a mean length of around 400–450 bp and subjected to library preparation using the NEBNext Ultra II DNA Library Prep Kit for Illumina (NEB), which included sequencing adapter addition and amplification. DNA Clean-up was performed using the Agencourt AMPure XP magnetic beads. All prepared libraries were sequenced using the Illumina NextSeq500 with the NextSeq 500/550 Mid Output Kit v2.5 (300 cycles), generating around 10 million paired-end 150-bp reads per sample.

Data processing. Sequencing reads were trimmed for both quality and adaptor sequences using cutadapt (v3.4)[59]. Trimmed reads were aligned to the GRCh38 reference genome using BWA Mem (v0.7.17-r1188)[53].

Identification of sequencing coverage. Sequencing read coverage per 50-bp bin was calculated using deeptools 'bamCoverage' (v3.5.1)[60] with default values. For visualization, the 50-bp read coverage values were combined into 10,000-bp bins using the function 'ScoreMatrixBin' of the genomation (v1.2.6) R package[61].

Validation of ecDNA breakpoint

VR01 and VR06 breakpoint sequences were inferred by AmpliconArchitect and used to design the following primers: VR01 forward (5′>3′): TACATGGGGCTCTGCTACCTGC; VR01 reverse (5′>3′): AGCCTGTCCCTTTTCCCACCCA; VR06 forward (5′>3′): TGCCTGCTTGTGTGAACTTGGCT; VR06 reverse (5′>3′): AGGTGGTGGGGGAGGCCTAAAA.

Breakpoint regions were amplified by PCR containing 30 ng of gDNA, 2.5 µl of buffer (Quantabio), 0.5 µl of 10 mM NTP Mix (Thermo Fisher Scientific), 1 µl of primers and 0.25 µl of AccuStart II Taq DNA polymerase (Quantabio) in a total volume of 25 µl. The PCR amplification cycling conditions were 95 °C for 2 min, followed by 35 cycles of 95 °C for 30 s, 65 °C for 30 s, and 72 °C for 30 s, with a final step at 72 °C for 5 min. PCR products were verified using the 5300 Fragment Analyzer (Agilent), purified using the ExoSAP-IT PCR Product Cleanup Reagent (Thermo Fisher Scientific) and sequenced by capillary electrophoresis using the BigDye Terminator v3.1 (Thermo Fisher Scientific) on the Applied Biosystems 3500dx Genetic Analyzer (Thermo Fisher Scientific). Sequencing data were aligned to the human genomic DNA using Primer-BLAST.

Droplet digital PCR

ddPCR was conducted on a QX200 ddPCR system (Bio-Rad Laboratories). For VR01 and VR06, the probes targeting the copy number variations (CNVs) were designed on the interconnected breakpoint of each ecDNA using Bio-Rad Laboratories software (https://www.bio-rad.com/digital-assays/assays-create/cnd). The breakpoints were previously inferred through AmpliconArchitect and validated via Sanger sequencing (Extended Data Fig. 1h). The other probes used were commercially

available (Bio-Rad Laboratories): *MYC* (FAM dHsaCP2500322), *EPHA3* (FAM dHsaCP52506272) and *TTC5* (HEX dHsaCP2506733) as reference genes for VR01 and VR06, and *EPHA3* (FAM dHsaCP52506272) and *PLEKHF1* (HEX dHsaCP2506723) as reference genes for VR23. Amplification was performed using the ddPCR Supermix for Probes, following the manufacturer's instructions (Bio-Rad Laboratories). Each reaction used 1 ng of genomic DNA in 20 µl of volume, containing probes (from 20X stock) and restriction enzyme (from 5 U μl^{-1}). The reaction was partitioned into approximately 20,000 droplets by an automated droplet generator according to the manufacturer's protocol (Bio-Rad Laboratories). The droplets were then transferred to a 96-well PCR plate and heat-sealed using the PX1 PCR plate sealer (Bio-Rad Laboratories). The PCR amplification cycling conditions were 95 °C for 10 min, followed by 40 cycles of 94 °C for 30 s and 60 °C for 60 s, and a final step at 98 °C for 10 min. After thermal cycling, each droplet was scanned using the QX200 Droplet Digital PCR system (Bio-Rad Laboratories). Positive and negative droplets in each fluorescent channel (HEX and FAM) were distinguished based on fluorescence amplitude, using a global threshold set by the minimal intrinsic fluorescence signal resulting from the imperfect quenching of the fluorogenic probes in negative droplets, compared with the strong fluorescence signal from cleaved probes in droplets with an amplified template (or templates). The QuantaSoft (v1.3.2.0) software was used to analyse CNVs.

Barcode sequencing

Genomic DNA was isolated as previously described and quantified using Qubit 4 Fluorometer (Thermo Fisher Scientific). We amplified the barcodes from the CloneTracker XP library and added the Illumina adaptors as well as unique sample index sequences for multiplex sequencing using the NGS Prep Kit for Barcode libraries in pScribe (LNGS-300). The first PCR was performed using 25 ng of genomic DNA and the following cycling conditions: 30 cycles of 95 °C and 65 °C for 30 s each and 68 °C for 2 min. An aliquot of 5 µl from the first-round PCR was used for the second-round PCR that was performed under the following cycling conditions: 12 cycles of 95 °C and 65 °C for 30 s each and 68 °C for 2 min. After quantification by Fragment Analyzer High Sensitivity NGS kit (Agilent Technologies), we first combined PCR products from each sample at the same amount, then we purified and concentrated the pool using Qiagen QIAquick PCR Purification Kit following the manufacturer's protocol. We quantified the library pools using NanoDrop spectrophotometer (Thermo Fisher Scientific) and then sequenced with custom read and index primers on the NextSeq2000 (Illumina), generating 150-bp paired-end reads at a depth of 5 million reads per sample. Of spiked-in PhiX control, 10% was sequenced by also adding the Standard Illumina primers to the custom read well.

Barcode sequencing analysis

Barcodes from genomic DNA sequencing were quantified using BWA (v0.7.18) and FeatureCounts from Rsubread package (v2.18.0). A FASTA reference file was first generated from the barcode pool provided by Cellecta. The sequencing reads were then aligned to the reference using the BWA-MEM (v0.7.17-r1188) algorithm. The resulting BAM files were subsequently used to quantify barcode abundances through the FeatureCounts functionality, as implemented in the R package Rsubread. To identify the presence of predominant barcodes, we selected those with a frequency exceeding 10% of the total barcode frequency within each condition.

DNA panel sequencing

Library preparation was performed using SureSelectXT HS Target Enrichment System (Agilent). Panel pair-end 2 × 150 sequencing was performed on NextSeq 550 (Illumina). Genes present in the panel are reported in Supplementary Table 3.

RNA sequencing

RNA from organoids were isolated using the TRIzol reagent (Life Technologies), followed by the column-based PureLink RNA Mini Kit (Thermo Fisher Scientific). Purified RNA quality was evaluated using the RNA 6000 Nano kit on a Bioanalyzer 2100 (Agilent), and only RNA with an RNA integrity number greater than 9 was used. The RNA sequencing library was obtained using poly(A) enrichment with the TrueSeq Stranded mRNA Library Prep kit (Illumina). Libraries obtained from PDOs at baseline ($n = 14$; analyses displayed in Fig. 1) were sequenced to a depth of 30 million fragments and 150-bp paired-end reads on an Illumina NextSeq 500 sequencer. For comparison between +WR and WRi PDOs, +WR PDOs were put in −WR for 24 h before RNA collection, to account for effect of the media. The resulting libraries were sequenced to a depth of 11 million fragments for organoids and 75-bp paired-end reads on an Illumina NextSeq 500 sequencer.

RNA sequencing analysis

Reads were aligned to the GRCh38 genome using STAR (v2.7), and the transcripts were quantified with RSEM (v1.3.3). For downstream analyses, the raw counts were normalized using the 'rlog' function of the DESeq2 R package. Genes with less than a total of 20 counts across all PDOs were removed before normalization. To compare gene expression values across amplicon types, the normalized gene values were *Z*-score normalized.

Tumour purity inference. The ESTIMATE (estimation of stromal and immune cells in malignant tumour tissues using expression data) tool was used to infer tumour purity of a subset of tumours from the ICGC ($n = 50$) and PDOs ($n = 14$) as previously described[62].

Gene set enrichment analysis. Differential gene expression analysis was conducted using 'DESeq2' (v1.34.0)[63]. $\log_2$ Fold-change shrinkage was applied using the 'lfcShrink' function in DESeq2 with the 'ashr' method[64]. Gene set enrichment analysis was performed using the 'fgsea' R package (v1.20.0)[65] with the Hallmark pathways database provided by the 'msigdbr' R package (v7.5.1)[66].

Subtyping. Subtyping was performed scoring the samples according to the Raghavan signatures[41] with the gene set variation analysis function (v1.42.0) and assigning the subtype according to what signature (basal or classical) achieved the highest score.

Fusion analysis. Fusion analysis was performed on adapted organoids to exclude the presence of chimeric proteins reactivating the WNT pathway. The nf-core/rnafusion (v3.0.0) pipeline was used to evaluate gene fusion from our RNA sequencing data; the pipeline was run under default parameters using all the fusion detection tools provided (arriba, fusioncatcher, pizzly, squid, starfusion and stringtie). Only fusions detected by at least two tools were considered as confident.

Xenium

Four patient FFPE tissues (ecDNA$^+$ $n = 2$ and ecDNA$^-$ $n = 2$) were characterized with Xenium (10X Genomics) in situ spatial transcriptomics using the Human Multi-tissue and Cancer panel (377 genes) plus a custom panel of 37 genes (Supplementary Table 6). FFPE samples were processed and analysed according to the manufacturer's protocol with no modifications. Post-Xenium H&E staining was performed as described in the Xenium protocols. We obtained a total of 807,253 cells, with a mean of 141.65 decoded transcripts for 100 μm^2, and good quality of transcripts (Phred quality score ≥ 20) above 92%. After quality control, we retained 805,966 cells for subsequent analysis. Raw Xenium data were imported in Seurat (v5.1.0) and integrated using reciprocal principal component analysis to remove batch effect correction. Cell clusters were identified with Leiden clustering at a resolution of 0.2, and

cluster markers were identified with R package presto (v1.0.0). Seurat cluster annotation was imported in Xenium Explorer (10X Genomics, v3.1.0) for visualization and integration with the H&E image.

Statistical analyses

All statistical analyses were carried out using R (v4.1.2) or GraphPad-Prism (v9.5.1). A Fisher's exact test and Chi-squared test were used to evaluate the significance in contingency tables. The Wilcoxon rank-sum test was used in two-group comparisons, and the relationship between two quantitative variables was measured using the Pearson correlation. Other statistical tests performed are described in the figures or in the figure legends.

Public datasets

Amplicon information for the ICGC PACA-CA and PACA-AU WGS samples was obtained from Kim et al.[21]. Additional matching ploidy data were retrieved from the ICGC Data Portal (https://dcc.icgc.org/releases/PCAWG). To focus on PDAC specifically, only PDAC tumours with histological types '8500/3', '8560/3', '8140/3', 'adenosquamous carcinoma' and 'pancreatic ductal adenocarcinoma' were used in the downstream analysis.

Reporting summary

Further information on research design is available in the Nature Portfolio Reporting Summary linked to this article.

Data availability

All processed data generated for this study are provided in the Supplementary tables. RNA sequencing data have been deposited in the Gene Expression Omnibus database under the accession code GSE247129. Barcode sequencing data have been deposited in the Gene Expression Omnibus database under the accession code GSE281325. WGS and CIRCLE-seq data generated in this study have been deposited in the European Genome-Phenome Archive (EGA) hosted by the EBI and CRG, under the accession numbers EGAS50000000193 and EGAS50000000194, respectively. Spatial transcriptomics data have been deposited in Zenodo[67]. Source data are provided with this paper.

51. Garcia, M. et al. Sarek: a portable workflow for whole-genome sequencing analysis of germline and somatic variants. *F1000Res.* **9**, 63 (2020).
52. Chen, S., Zhou, Y., Chen, Y. & Gu, J. fastp: An ultra-fast all-in-one FASTQ preprocessor. *Bioinformatics* **34**, i884–i890 (2018).
53. Li, H. Aligning sequence reads, clone sequences and assembly contigs with BWA-MEM. Preprint at https://arxiv.org/abs/1303.3997 (2013).
54. McKenna, A. et al. The Genome Analysis Toolkit: a MapReduce framework for analyzing next-generation DNA sequencing data. *Genome Res.* **20**, 1297–1303 (2010).
55. Talevich, E., Shain, A. H., Botton, T. & Bastian, B. C. CNVkit: genome-wide copy number detection and visualization from targeted DNA sequencing. *PLoS Comput. Biol.* **12**, e1004873 (2016).
56. Luebeck, J. et al. Extrachromosomal DNA in the cancerous transformation of Barrett's oesophagus. *Nature* **616**, 798–805 (2023).
57. Priestley, P. et al. Pan-cancer whole-genome analyses of metastatic solid tumours. *Nature* **575**, 210–216 (2019).
58. Koche, R. P. et al. Extrachromosomal circular DNA drives oncogenic genome remodeling in neuroblastoma. *Nat. Genet.* **52**, 29–34 (2020).
59. Martin, M. Cutadapt removes adapter sequences from high-throughput sequencing reads. *EMBnet.journal* https://doi.org/10.14806/ej.17.1.200 (2011).
60. Ramirez, F., Dundar, F., Diehl, S., Gruning, B. A. & Manke, T. deepTools: a flexible platform for exploring deep-sequencing data. *Nucleic Acids Res.* **42**, W187–W191 (2014).
61. Akalin, A., Franke, V., Vlahovicek, K., Mason, C. E. & Schubeler, D. Genomation: a toolkit to summarize, annotate and visualize genomic intervals. *Bioinformatics* **31**, 1127–1129 (2015).
62. Yoshihara, K. et al. Inferring tumour purity and stromal and immune cell admixture from expression data. *Nat. Commun.* **4**, 2612 (2013).
63. Love, M. I., Huber, W. & Anders, S. Moderated estimation of fold change and dispersion for RNA-seq data with DESeq2. *Genome Biol.* **15**, 550 (2014).
64. Stephens, M. False discovery rates: a new deal. *Biostatistics* **18**, 275–294 (2017).
65. Korotkevich, G. et al. Fast gene set enrichment analysis. Preprint at *bioRxiv* https://doi.org/10.1101/060012 (2021).
66. Liberzon, A. et al. Molecular signatures database (MSigDB) 3.0. *Bioinformatics* **27**, 1739–1740 (2011).
67. Corbo, V. & Rosa, D. ecDNA amplification of MYC drives intratumor copy-number heterogeneity and adaptation to stress in PDAC. *Zenodo* https://doi.org/10.5281/zenodo.14051632 (2025).

Acknowledgements We acknowledge the Centro Piattaforme Tecnologiche (University of Verona) for granting access to the genomic and imaging facilities of the University of Verona; the GSTEP, Multiplex spatial profiling facility and Bioinformatics Research Core Facility. This article is dedicated to the memory of Claudio Bassi, an inspiring figure for pancreatic cancer researchers worldwide; and to the memory of Laura Ziliani, who lost her life to pancreatic cancer and has greatly supported pancreatic cancer research through the Fondazione Nadia Valsecchi. V.C. is supported by the Associazione Italiana Ricerca sul Cancro (AIRC; Start-up grant no. 18178 and IG no. 28801), and the National Cancer Institute (HHSN26100008) and Fondazione Nadia Valsecchi. This work has been supported in part by 'Finanziamento dell'Unione Europea-Next Generation EU, Missione 4, Componente 1 CUP B53D23024740001'. V.C., A.M., D.S., P.B. and C.P. are supported by the EU (MSCA project PRECODE, grant no. 861196). A. Scarpa is supported by the AIRC (26343). C.C. is supported by the AIRC (My First AIRC grant no. 23681). E.F. is supported by the AIRC (25286 and 29692). M.B. is supported by the AIRC (28054 and 29829). L.V. is supported by the AIRC (29528). P.B. and V.C. are supported by the Würth foundation. The funding agencies had no role in the collection, analysis and interpretation of data or in the writing of the manuscript.

Author contributions E.F., A.M., D.S., P.B. and V.C. conceived and designed the research. S.D. and S.A. established the human organoid cultures. A.M., E.F. and G.A. performed the experiments with organoids. E.F., A.M. and S.P. performed the FISH experiments. E.F., A.M., M.B., F.L. and L.V. performed the immunostaining experiments. M.B. performed the panel DNA sequencing, validated the ecDNA breakpoints and performed the ddPCR. D.S., D.P., D.R. and P.B. analysed the omics data and generated displays. C.N. assisted with the CIRCLE-seq analysis. C.C., A.A., D.R. and D.P. generated and analysed the spatial transcriptomics data. A. Sottoriva, L.A., M.C. and S.M. assisted with barcoding and barcode sequencing. R.T.L., R.S., G.M., A.R., A.G., M.M. and S.G. collected samples, and provided tissue annotation and clinicopathological information. A. Scarpa and C.L. performed the histopathological evaluation of human tissues. E.F., A.M., D.S., P.B. and V.C. interpreted the data with assistance from D.A.T. and C.P. E.F., A.M., D.S., P.B. and V.C. wrote the manuscript. V.C., P.B. and D.A.T. supervised the study. All authors approved the final version of the manuscript.

Competing interests The authors declare no competing interests.

Additional information

Supplementary information The online version contains supplementary material available at https://doi.org/10.1038/s41586-025-08721-9.

Correspondence and requests for materials should be addressed to Peter Bailey or Vincenzo Corbo.

Peer review information *Nature* thanks Benjamin Werner and the other, anonymous, reviewer(s) for their contribution to the peer review of this work. Peer reviewer reports are available.

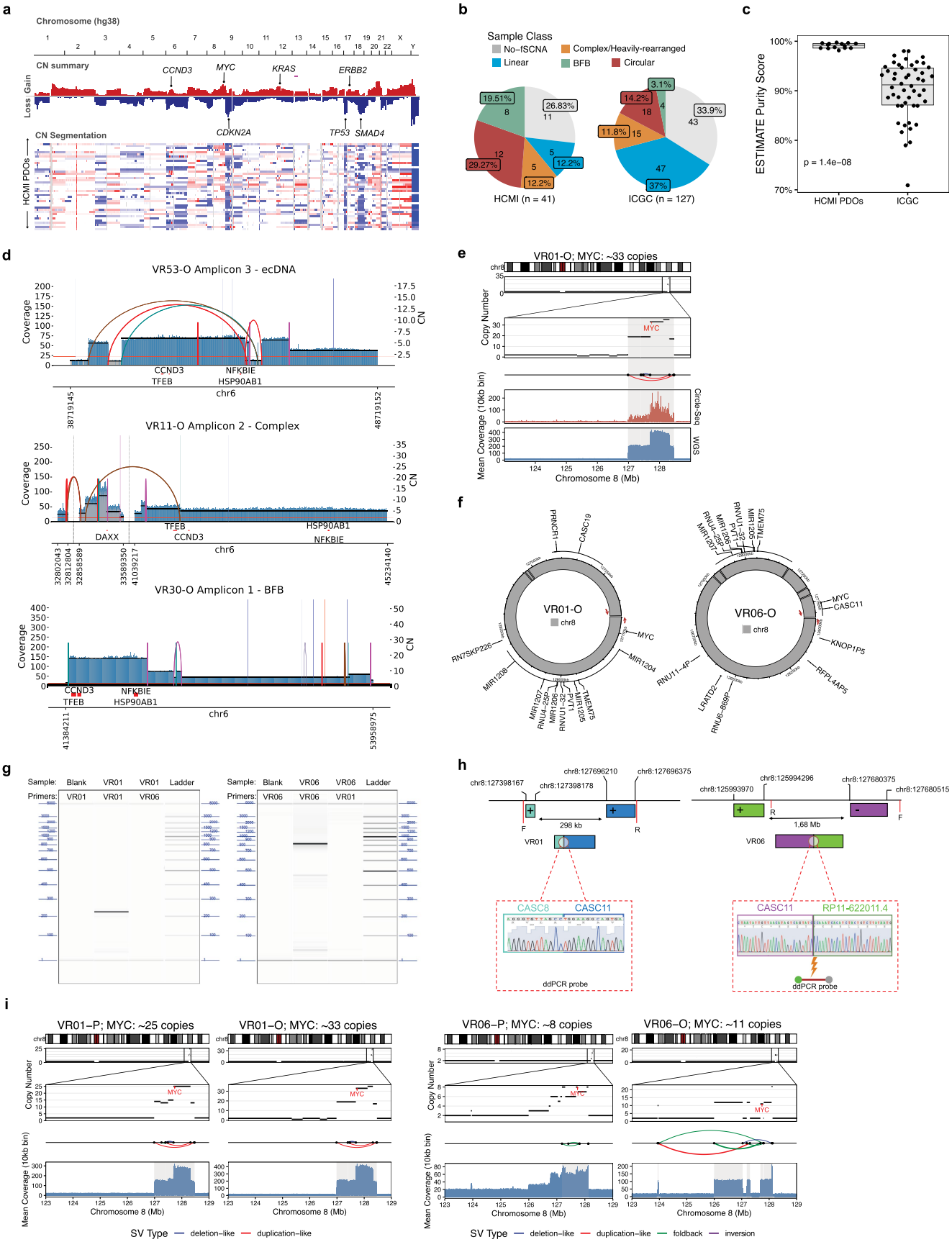

Extended Data Fig. 1 | See next page for caption.

Extended Data Fig. 1 | EcDNA based amplifications in PDAC. a, Copy number (CN) analysis showing: top panel, CN frequency plot displaying the frequency of copy number gains (0.1) and losses (-0.1) observed across the genome (segmentation mean) for the HCMI PDOs (Verona cohort). Representative genes are shown on the plot at their genomic location; bottom panel, CN calls for individual samples. Red represents CN gain and blue represents CN loss. **b**, Pie charts showing proportion of primary tumours (ICGC) and PDOs (HCMI) falling in each sample class based on their existing amplicon types. If a sample contained multiple amplicons, it was classified based on the following order: Circular > BFB > Complex > Linear. If no amplicon was detected, the sample was classified as no-focal somatic copy number amplification detected (No-fSCNA). **c**, Distribution of ESTIMATE[62] purity score in a subset of samples from the PDOs and the ICGC cohorts. The box plots show the median (centre line), upper and lower quartiles (box limits), and 1.5× interquartile range (whiskers). PDOs: n = 14; ICGC: n = 50. Statistical significance was evaluated using a two-sided Wilcoxon rank sum test. **d**, Structural variant (SV) view of AA reconstructed amplicon structures containing the *CCND3* locus for three PDOs with different amplicon classifications. SV view shows coverage depth, copy number segments and discordant genomic connections (curves spanning copy number segments). **e**, Validation of the presence of *MYC* on ecDNA by Circle-Seq for VR01-O. **f**, Representative Circos plots showing amplicon regions identified by AA in VR01-O and VR06-O for the ecDNAs containing *MYC*. Red arrows indicate the interconnected breakpoints for which primer pairs were designed. **g**, Gel-like image showing the size-based separation of the regions spanning the interconnected breakpoints of the circular amplicons detected in VR01-O and VR06-O. The primer pairs used are indicated in panel f. **h**, Capillary sequencing traces generated from the purified products (displayed in **g**). The chromosomal coordinates and strand orientation of the two loci spanning the interconnected breakpoints are shown in the schematic (top panel). **i**, Copy number alterations on chromosome 8 with a focus on *MYC* region of primary tissues (P) and matched organoids (O) for VR01 (left) and VR06 (right). SVs that connect amplified regions and form ecDNAs are displayed below copy number levels. WGS Coverage is depicted at the bottom.

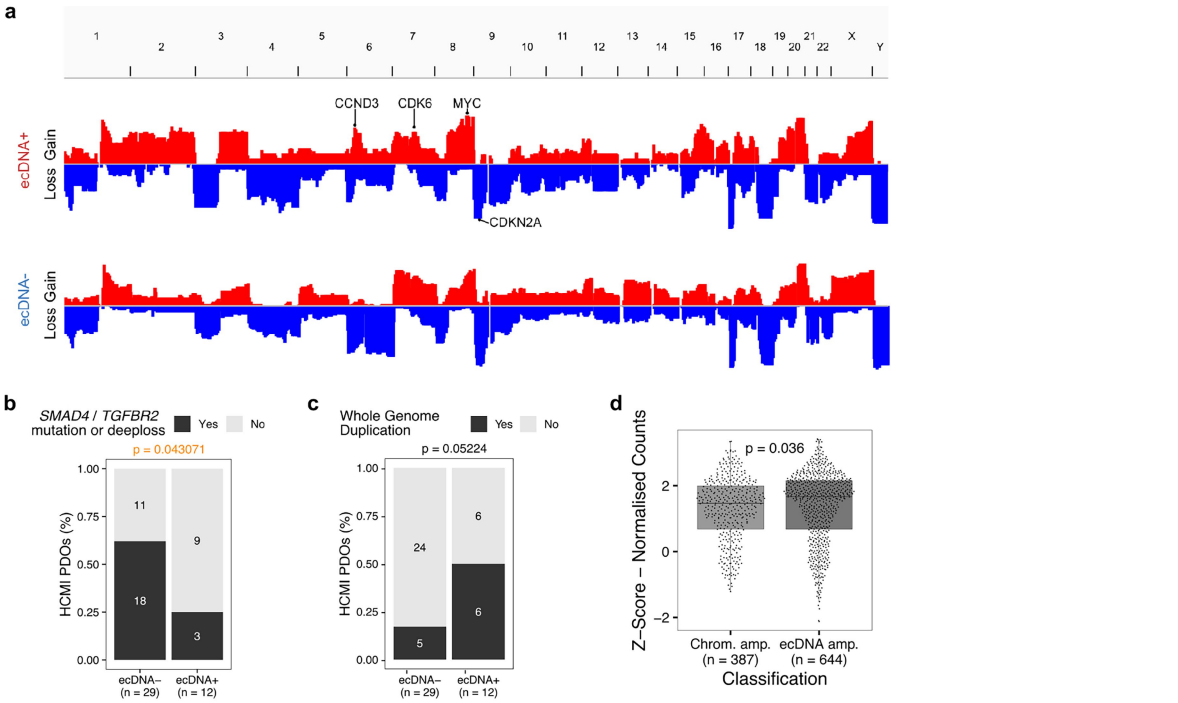

Extended Data Fig. 2 | Extrachromosomal amplifications are associated with features of advanced disease. a, CN frequency plot showing gains (red) and losses (blue) for ecDNA+ (n = 12) and ecDNA- (n = 29) organoids. *CDKN2A* was found to be lost in 10/12 ecDNA+ organoids in comparison to 14/29 ecDNA- organoids (p value = 0.0026). *CCND3* gain was more common in ecDNA+ organoids (5/12) than ecDNA- organoids (1/29) (p value = 0.0053) and *CDK6* gain was identified in 4/12 ecDNA+ and 2/29 ecDNA- organoids (p value = 0.05). Loss: copy number ≤ 1; Gain: copy number ≥ 3. P values were calculated using a two-sided Fisher's exact test. **b**, Bar plot showing enrichment for *SMAD4/TGFBR2* inactivating mutations or deep loss in ecDNA- HCMI PDOs. P value was calculated using a two-sided Fisher's exact test **c**, Bar plot displaying enrichment of whole genome duplication in ecDNA+ HCMI PDOs. P value was calculated using a two-sided Fisher's exact test. **d**, Boxplot showing normalised expression of genes (Z-scores) located on circular amplicons (ecDNA amp) or chromosomally amplified (chrom amp). The box plots show the median (centre line), upper and lower quartiles (box limits), and 1.5× interquartile range (whiskers). Chrom. Amp.: n = 387; ecDNA amp.: n = 644. Statistical significance was evaluated using a two-sided Wilcoxon rank sum test.

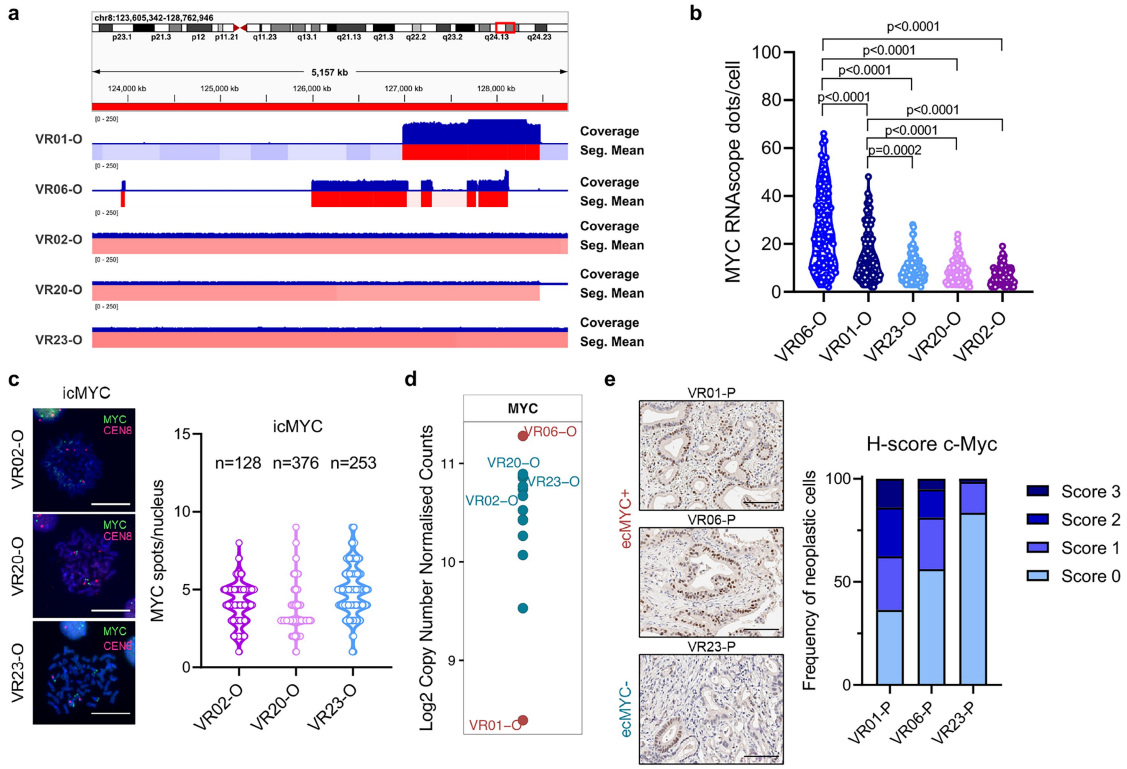

Extended Data Fig. 3 | *MYC* copy number heterogeneity in PDAC. a, Coverage and segmentation mean histograms spanning the *MYC* locus for the samples indicated. **b**, Quantification of mRNA expression, as number of dots/cells, in ecDNA+ (VR01-O, VR06-O) and ecDNA- (VR23-O, VR20-O, VR02-O) organoids. At least 100 individual cells per culture were analyzed. P values determined by One-way ANOVA, using the Sidak's multiple comparison test. **c**, Representative FISH images of metaphases from *icMYC* PDOs. Scale bar: 20 µm (left). On the right, quantification of *MYC* copy-number per nucleus (number of nuclei analysed: VR02 n = 128, VR20 n = 376, VR23 n = 253). **d**, *MYC* expression values normalised by copy-number of *ecMYC*+ PDOs (red) and *ecMYC*- PDOs (blue). **e**, Representative immunohistochemistry for c-Myc in VR01, VR06, and VR23 patients' primary tumours. Scale bar: 100 µm (left). Quantification is provided on the right as distribution of H-scores per tissue. At least 1000 cells were analysed for each case.

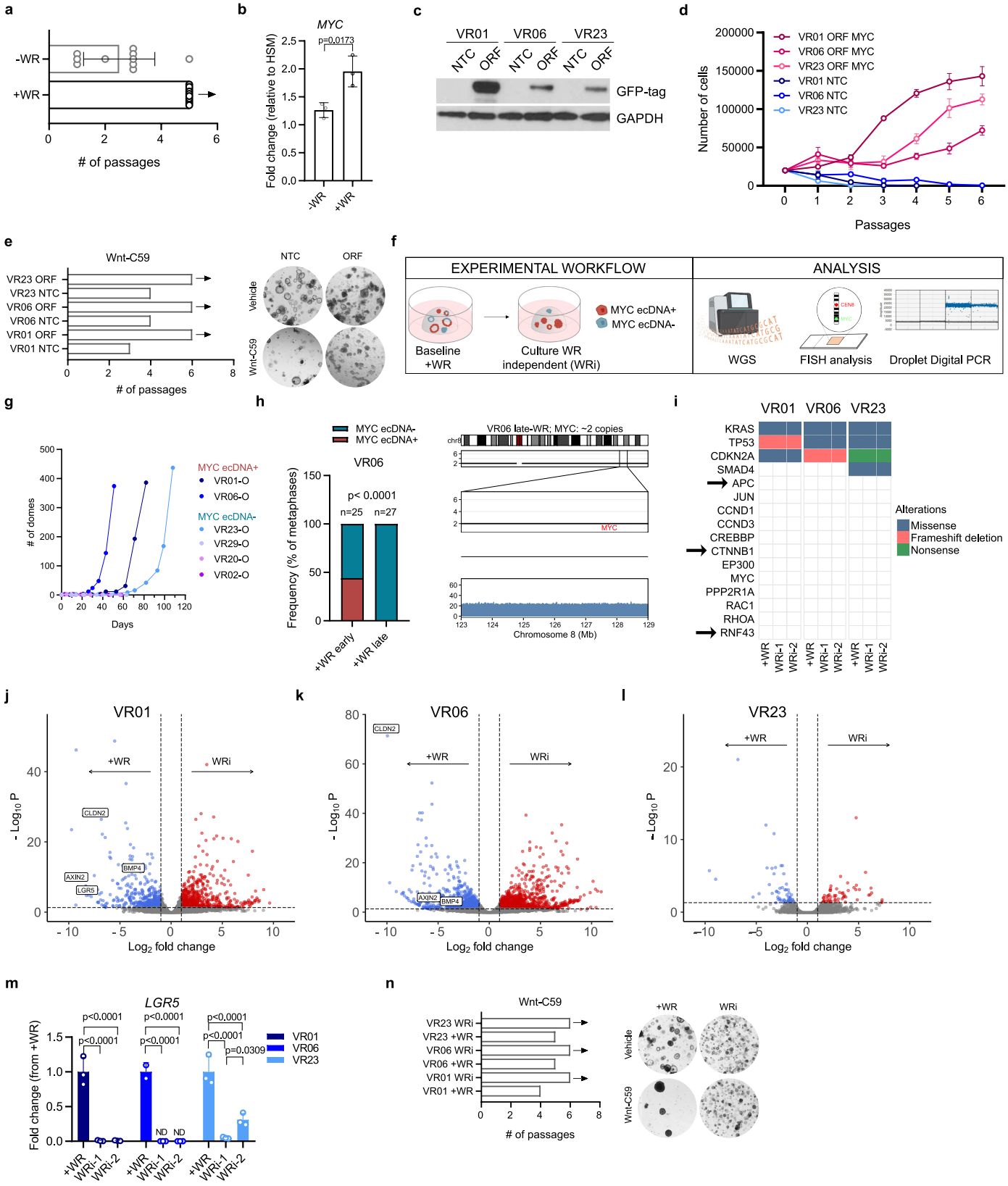

Extended Data Fig. 4 | See next page for caption.

Extended Data Fig. 4 | Elevated *MYC* activity drives adaptation to a WNT deficient environment. a, Bar plot showing mean ± SD of number of passages at which organoid cultures (n = 9) passaged every week with a splitting ratio of 1:3 in -WR media reach extinction, compared to +WR media. The arrow indicates that the culture could be propagated indefinitely. **b**, Changes in relative expression levels of *MYC* of starved organoids (HSM), after culture in -WR, and +WR media for 8 h. Results shown as mean ± SD of three biological replicates (VR01, VR02, and VR23). P value was determined by Student's two tailed t-test. *GAPDH* was used as a housekeeping control gene to normalise results. **c**, Immunoblot analysis of GFP-tag in whole cell lysate of VR01-O, VR06-O and VR23-O transduced with NTC (non-targeting control) and a GFP-tagged Myc ORF (open reading frame). GAPDH was used as loading control. **d**, Cell proliferation of parental (NTC) and MYC overexpressing (ORF) cultures over six passages in -WR medium. Cells were passaged weekly, and cell counts were measured at each passage. Results are expressed as the mean ± SD of three technical replicates for each condition. **e**, Bar plot showing the number of passages at which each organoid culture could be propagated in the presence of Wnt-C59 (100 nm, PORCN inhibitor). The arrows indicate that the culture could be propagated indefinitely (left). Representative brightfield images of parental (NTC) and MYC overexpressing cultures (ORF) cultivated in the absence (vehicle) or in the presence (Wnt-C59) of the PORCN inhibitor (right). **f**, Schematic representation of the experimental workflow. Created in BioRender. Corbo, V. (2025) https://BioRender.com/v05m748. **g**, Growth curve of *MYC* ecDNA+ (n = 2) and *MYC* ecDNA- (n = 4) organoids in -WR media. Culture growth is represented as number of domes (50 µl Matrigel/dome). **h**, Frequency of ecDNA+ metaphases for VR06-O cultured in +WR medium at early (n = 25) and late passages (n = 27). P value as determined by two-sided Chi-square (left). Copy number alterations on chromosome 8 (with a focus on *MYC* region) of VR06 late passage after few passages in depleted media (-WR). WGS coverage is displayed below the copy number level (right). **i**, Oncoplot displaying absence of mutations in genes involved in WNT pathway that could explain the acquisition of WR independence of WRi organoids. The arrows indicate WNT pathway genes commonly altered in cancers. **j-l**, Volcano plots showing differentially expressed genes between parental and WRi cultures. Upregulated genes are showed as red dots (padj < 0.05 and log2foldchange > 1). Downregulated genes are showed as blue dots (padj < 0.05 and log2foldchange < -1). P adjusted is calculated by two-sided Wald test with Benjamini-Hochberg correction. Canonical WNT target genes are indicated. **m**, Changes in the relative expression levels of *LGR5* in WRi organoids compared to parental cultures (+WR). Results shown as mean ± SD of three technical replicates. Significance was determined by Two-way ANOVA with Tukey's multiple comparisons test. *HPRT1* was used as a control. ND, not determined. **n**, Bar plot showing the number of passages at which each organoid could be propagated in the presence of Wnt-C59 (left). Representative brightfield images of parental (+WR) and WRi organoids cultured in the presence of Wnt-C59 (100 nM, PORCN inhibitor) or appropriate vehicle (right).

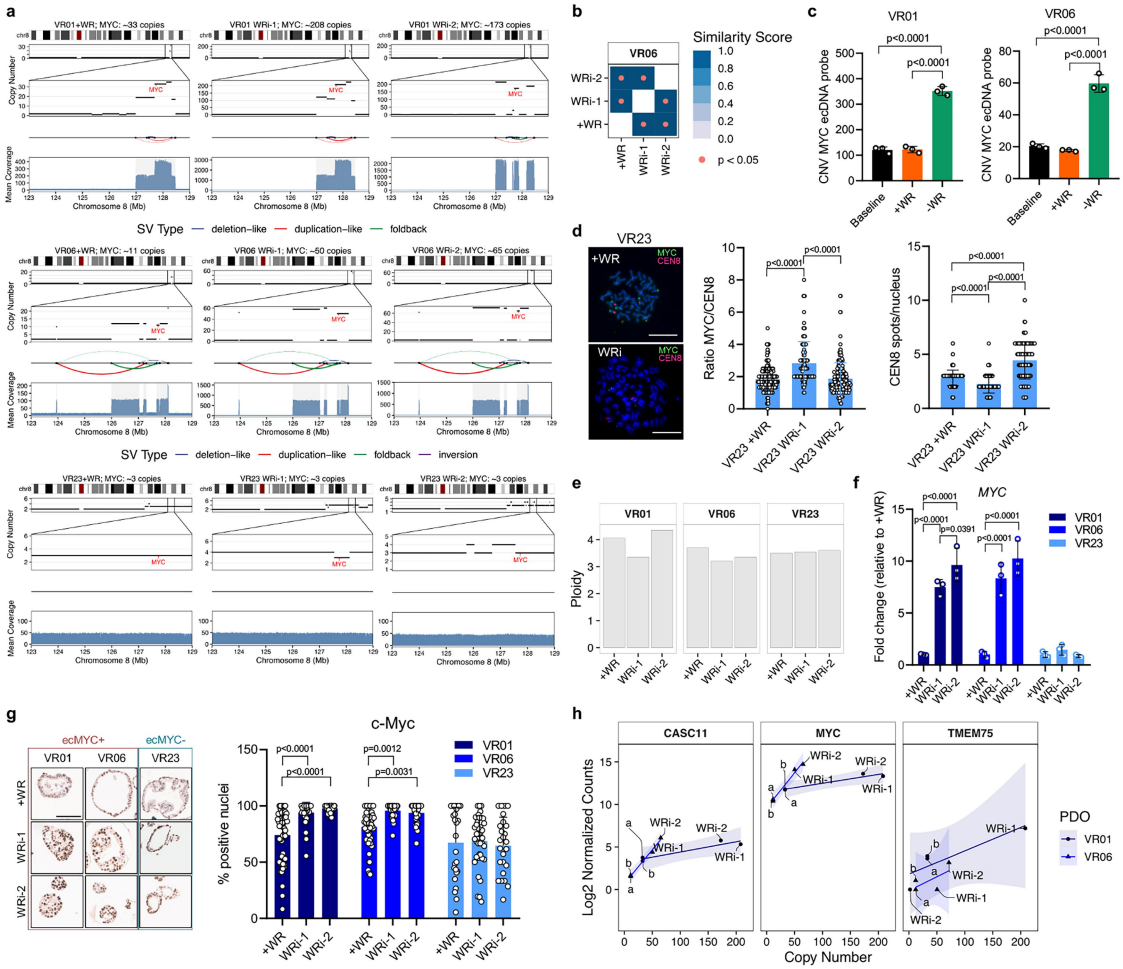

Extended Data Fig. 5 | Changes in *MYC* copy-number and expression following emergence of the WRi phenotype. a, Copy number alterations on chromosome 8 with a focus on *MYC* region, of VR01-O (top), VR06-O (middle), and VR23-O (bottom) cultures at baseline (+WR) and following acquisition of the WRi phenotype (WRi, two biological replicates). SVs that connect amplified regions and form ecDNA and WGS Coverage are displayed below the copy number levels. **b**, Similarity score[56] of the circular amplicons containing *MYC* for VR06-O cultures across conditions suggesting common origins for the structures. The p value was calculated by the similarity score program. **c**, Quantification of *ecMYC* copy-number by ddPCR for both VR01-O and VR06-O at baseline and following cultivation in medium supplemented with (+WR) or depleted of (-WR) WNT agonists. Data are presented as mean of 3 biological replicates ± SD. P values were calculated using One-way ANOVA with Tukey's multiple comparisons test. **d**, Representative FISH metaphases of VR23-O at baseline (+WR) and after acquisition of the WRi phenotype. Scale bar: 20 µm (left). Bar plot showing the ratio of *MYC* signal over *CEN8* (middle) and the number of *CEN8* spots (right) in VR23 at baseline (n = 250) and after WR independence (two biological replicates: WRi-1 n = 101, WRi-2 n = 197). Data are presented as mean ± SD. P values by One-way ANOVA with Holm-Sidak's multiple comparisons test. **e**, Ploidy analysis of organoids at baseline (+WR) and after acquisition of the WRi phenotype. Ploidy was assessed from the WGS data using AMBER, COBALT, and PURPLE in tumor only mode (https://github.com/hartwigmedical/hmftools). **f**, Changes in the relative expression levels of *MYC* in WRi organoids compared to parental cultures. Results shown as mean ± SD of three replicates. P value determined by Two-way ANOVA with Tukey's multiple comparisons test. *GAPDH* was used as housekeeping control gene to normalise results. **g**, Representative immunohistochemistry for c-Myc of formalin-fixed paraffin-embedded organoids at baseline and adapted to grow in -WR media. Scale bar: 100 µm (left). Quantification is provided on the right as frequency of positive nuclei per organoid. A minimum of 25 organoids per sample were analysed. Data are presented as mean ± SD. P values determined by Two-way ANOVA with Tukey's multiple comparisons test. **h**, Copy number and expression levels of the genes *MYC*, *CASC11*, and *TMEM75*, in parental (a, b) and WRi cultures. Grey area represents 95% confidence interval.

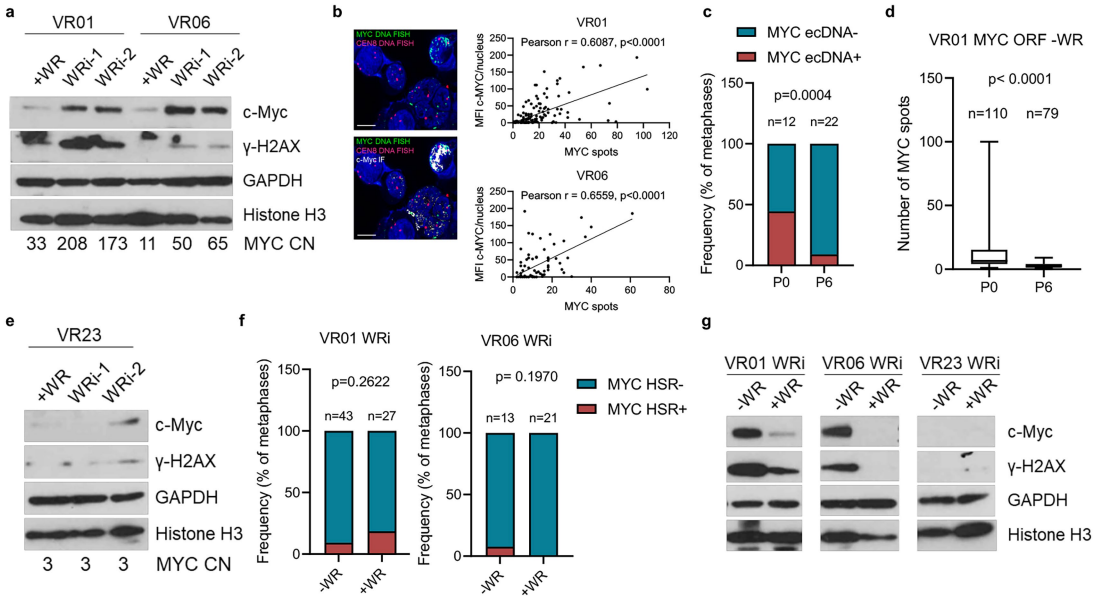

Extended Data Fig. 6 | Accumulation of ecDNA is associated with increased γH2AX foci. a, Immunoblot analysis in whole cell lysate of *ecMYC* organoids at baseline (+WR) and following emergence of the WRi phenotype (2 biological replicates). GAPDH and Histone H3 were used as loading controls. *MYC* CN: WGS-based copy number. Conducted n = 1. **b**, Immuno-FISH analysis for *MYC/CEN8* and MYC protein in ecDNA+ PDOs. Scale bar, 10 µm (left). Scatter plot showing the Pearson's r correlation of MYC protein level and *MYC* copy-number. Individual nuclei were quantified (VR01 n = 146, VR06 n = 115). Two-tailed p value was obtained from r correlation test (right). **c**, The stacked bar plots show the changes in the frequency of *MYC* ecDNA+ metaphases of VR01-O overexpressing MYC following cultivation in WNT-depleted medium (P0: n = 12; P6: n = 22). P values determined by two-sided Chi-square. **d**, Quantification of *MYC* copy-number in VR01-O overexpressing MYC (ORF) following cultivation in WNT-depleted medium. The box plots show the median (centre line), upper and lower quartiles (box limits), and 1.5× interquartile range (whiskers). P0: n = 110, P6: n = 79. P values determined by Wilcoxon rank sum two-sided test. **e**, Immunoblot analysis of VR23-O at baseline (+WR) and following emergence of the WRi phenotype (2 biological replicates). GAPDH and Histone H3 were used as loading controls. *MYC* CN: WGS-based copy number. Conducted n = 1. **f**, Stacked bar plots showing changes in the frequency of HSR+ metaphases in VR01-O and VR06-O WRi following re-introduction of WNT agonists in the culture medium (VR01 WRi: -WR n = 43, +WR n = 27; VR06 WRi: -WR n = 13, +WR n = 21). P values determined by Fisher's exact two-sided test. **g**, Immunoblot analysis in whole cell lysates of WRi cultures cultivated in the absence and presence (+WR) of WNT agonists. GAPDH and Histone H3 were used as loading controls. Conducted n = 1.

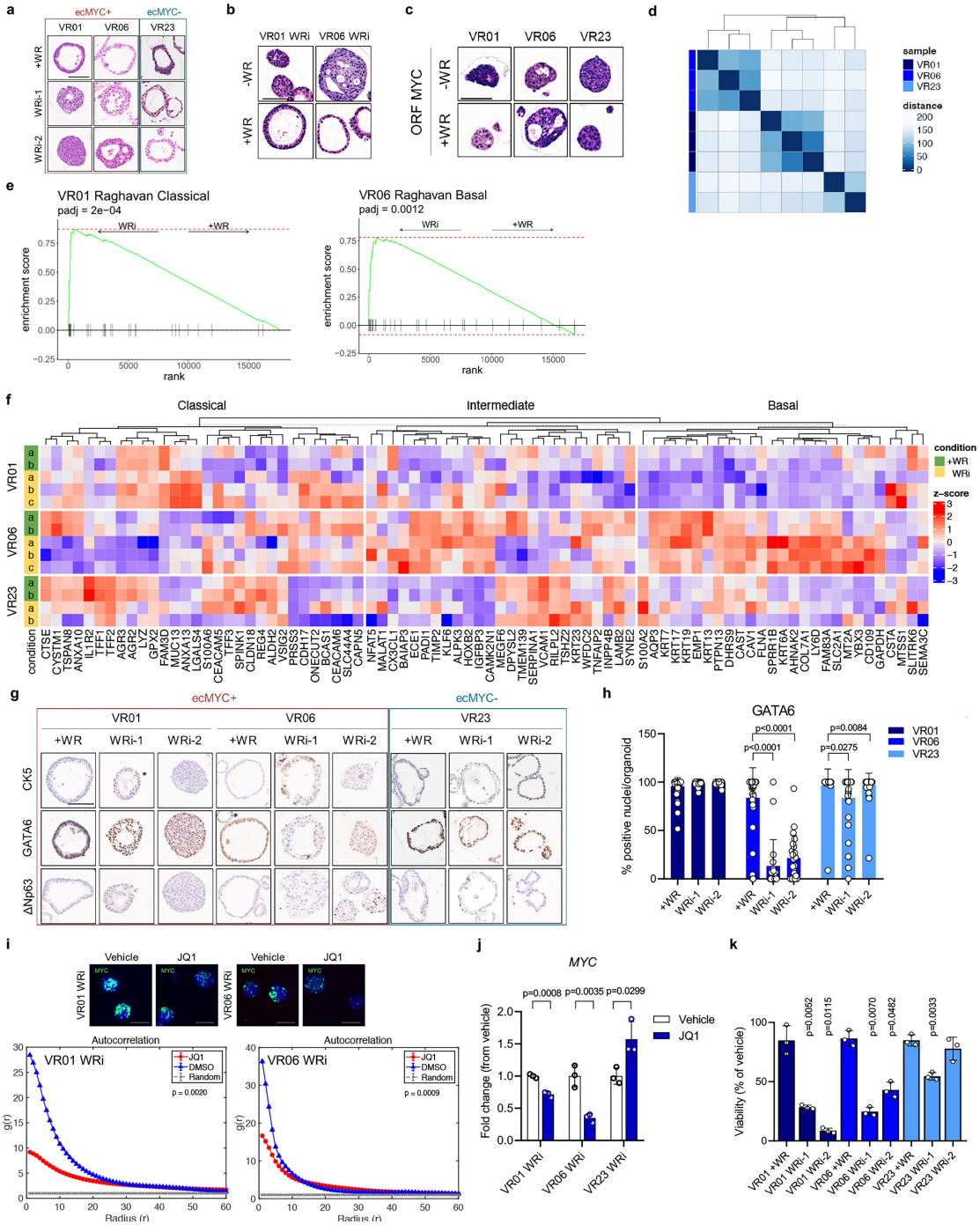

Extended Data Fig. 7 | Accumulation of ecDNA is associated with morphological and phenotypic changes. a, Representative Haematoxylin and Eosin (H&E) staining of formalin-fixed paraffin-embedded organoids at baseline and after WRi. Scale bar: 100 µm. Conducted n = 3. **b**, Representative H&E staining demonstrating reversibility of morphological changes of WRi cultures following reintroduction of WNT agonists in the culture medium. Scale bars, 100 µm. Conducted n = 1. **c**, Representative H&E staining demonstrating the irreversibility of morphological changes induced by the acquisition of the WRi phenotype due to exogeneous overexpression of MYC (ORF). Scale bars, 100 µm. Conducted n = 1. **d**, Similarity heatmap based on the Euclidean sample distance. **e**, Gene set enrichment analysis (GSEA). Left panel, enrichment of Classical geneset computed over the ranked lists of VR01 differentially expressed genes, derived from the comparison of WRi and parental cultures. Right panel, enrichment of Basal geneset computed over the ranked lists of VR06 differentially expressed genes, derived from the comparison of WRi and parental cultures. P adjusted was calculated using Permutation test with Benjamini-Hochberg correction. **f**, Heatmap displaying the expression of Classical, Intermediate, and Basal genes from Raghavan et al.[41] in parental and WRi organoids. **g**, Representative immunohistochemistry for cytokeratin 5 (CK5), GATA6, and ΔNp63 of parental (+WR) and WRi organoids. Scale bar: 100 µm. Quantification for GATA6 is provided in **h** as mean frequency ± SD of GATA6+ nuclei per organoid, at least 20 organoids were analysed for each condition. P values were calculated by Two-way ANOVA with Tukey's multiple comparisons test. **i**, Representative FISH interphase nuclei of WRi organoids treated with JQ1 (500 nM) or appropriate vehicle control for 72 h showing reduction of *MYC* hubs upon treatment. Scale bar: 20 µm (top). Interphase signal clustering measured by autocorrelation g(r)[28] in WRi cultures treated with JQ1 or vehicle (DMSO) for 72 h. P values determined by two-sided Wilcoxon test at r = 0. **j**, Changes in the relative expression levels of *MYC* in WRi organoids treated with JQ1 (500 nM) for 72 h. P value determined by Two-way ANOVA. Results shown as mean ± SD of three replicates. *GAPDH* was used as housekeeping control gene to normalise results. **k**, Bar plot showing mean of three technical replicates ± SD of cell viability of parental (+WR) and WRi organoids upon 72 h of JQ1 treatment (500 nM). P value determined by paired two-tailed Student's t test.

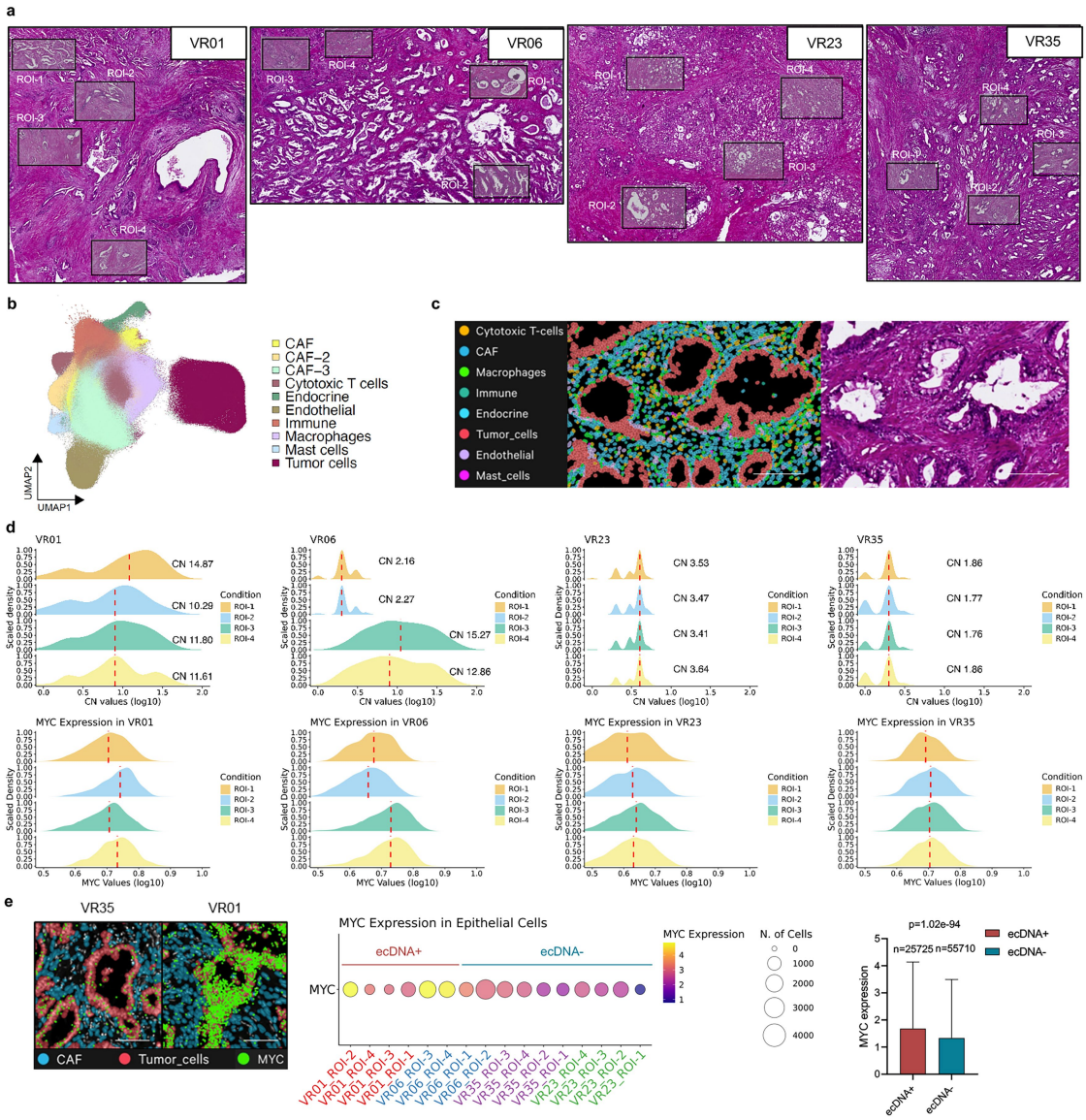

Extended Data Fig. 8 | Integrated spatial transcriptomics and cytogenetic analysis of PDAC tissues. a, Post Xenium H&E of 4 PDAC tissues with annotation of the regions of interest (ROIs) selected for analysis. **b**, UMAP plot showing the 10 annotated Xenium clusters. **c**, Spatial plot showing mapping of the annotated clusters (left) along with the post-xenium H&E (right). Scale bar, 100 µm. **d**, Distribution of *MYC* copy-number (top) and *MYC* expression levels (bottom) per cell in the 4 ROIs selected for each of the PDAC tissues. The average CN for each ROIs is provided. The red dashed line indicates the median value. **e**, Spatial plot showing localization and levels of *MYC* mRNA in tumor cells of VR35 (ecDNA-) and VR01 (ecDNA+). Scale bars, 100 µm (left). Bubble plot of the scaled average expression of *MYC* in epithelial cells. The colour intensity represents the expression level, and the size of the bubbles represents the percentage of expressing cells (middle). Quantification as mean ± SD *MYC* expression of cells in ecDNA+ (n = 25725) and ecDNA- (n = 55710) areas. P values determined by Wilcoxon test (two-sided) (right).

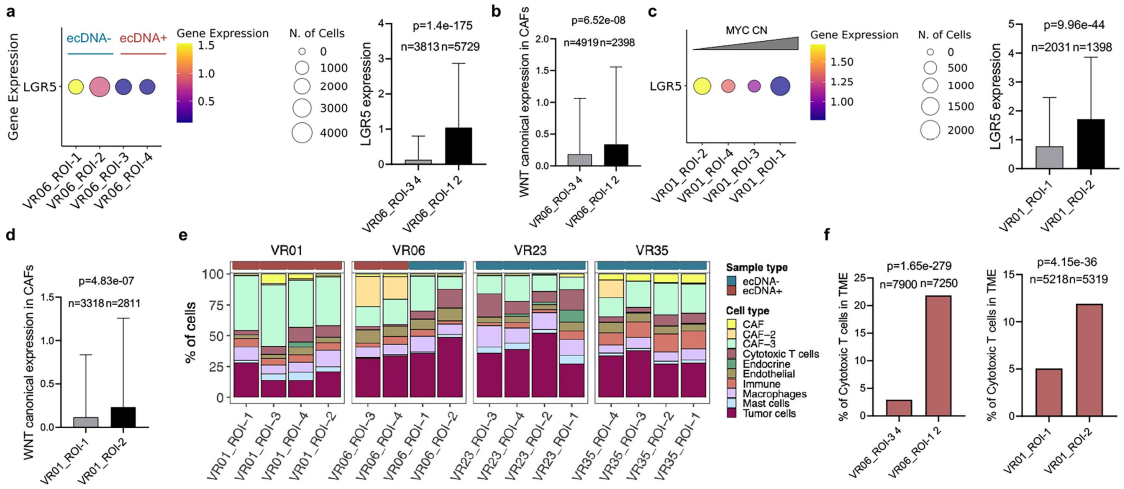

Extended Data Fig. 9 | Immune territory of *MYC* amplified cells. a, Bubble plot of the scaled average expression of *LGR5* in epithelial cells of VR06. The colour intensity represents the expression level, and the size of the bubbles represents the number of expressing cells (left). Quantification of *LGR5* expression in epithelial cells is provided on the right as mean ± SD of ROIs 3 and 4 (n = 3813) and ROIs 1 and 2 (n = 5729) of VR06. P values determined by Wilcoxon test (two-sided). **b**, Quantification of the WNT canonical ligand expression in CAFs as mean ± SD in ROIs 3 and 4 (n = 4919) and ROIs 1 and 2 (n = 2398) of VR06. P values determined by Wilcoxon test (two-sided). **c**, Bubble plot of the scaled average expression of *LGR5* in epithelial cells of VR01. The colour intensity represents the expression level, and the size of the bubbles represents the number of expressing cells (left). Quantification of *LGR5* expression in epithelial cells is provided on the right as mean ± SD of ROI 1 (n = 2031) and ROI 2 (n = 1398) of VR01. P values determined by Wilcoxon test (two-sided) (right). **d**, Quantification of WNT canonical ligands expression in CAFs as mean ± SD of ROI 1(n = 3318) and ROI 2 (n = 2811) of VR01. P values determined by Wilcoxon test (two-sided). **e**, Frequency of the annotated cell types across selected ROIs for each PDAC tissue. Areas containing *MYC* amplified cells (ecDNA+) are indicated. **f**, Proportion of cytotoxic T cells (*CD8* expressing cells) per case stratified by presence or absence of *MYC* amplification. Statistical significance by Chi square (two-sided).

nature portfolio

Corresponding author(s): Vincenzo Corbo, Peter Bailey

Last updated by author(s): Dec 20, 2024

Reporting Summary

Nature Portfolio wishes to improve the reproducibility of the work that we publish. This form provides structure for consistency and transparency in reporting. For further information on Nature Portfolio policies, see our Editorial Policies and the Editorial Policy Checklist.

Statistics

For all statistical analyses, confirm that the following items are present in the figure legend, table legend, main text, or Methods section.

n/a	Confirmed	
☐	☒	The exact sample size (*n*) for each experimental group/condition, given as a discrete number and unit of measurement
☐	☒	A statement on whether measurements were taken from distinct samples or whether the same sample was measured repeatedly
☐	☒	The statistical test(s) used AND whether they are one- or two-sided *Only common tests should be described solely by name; describe more complex techniques in the Methods section.*
☐	☒	A description of all covariates tested
☐	☒	A description of any assumptions or corrections, such as tests of normality and adjustment for multiple comparisons
☐	☒	A full description of the statistical parameters including central tendency (e.g. means) or other basic estimates (e.g. regression coefficient) AND variation (e.g. standard deviation) or associated estimates of uncertainty (e.g. confidence intervals)
☐	☒	For null hypothesis testing, the test statistic (e.g. *F*, *t*, *r*) with confidence intervals, effect sizes, degrees of freedom and *P* value noted *Give P values as exact values whenever suitable.*
☒	☐	For Bayesian analysis, information on the choice of priors and Markov chain Monte Carlo settings
☒	☐	For hierarchical and complex designs, identification of the appropriate level for tests and full reporting of outcomes
☐	☒	Estimates of effect sizes (e.g. Cohen's *d*, Pearson's *r*), indicating how they were calculated

Our web collection on statistics for biologists contains articles on many of the points above.

Software and code

Policy information about availability of computer code

Data collection	Hematoxylin and Eosin and Immunohistochemistry slides were scanned and digitalised using the Aperio Scan-Scope XT Slide Scanner (Aperio Technologies). Immunofluorescence and FISH images were acquired either on Leica TCS SP5 Fluorescent microscopes (Leica Application Suite X (LAS X) software) or on Olympus Life Science FV4000 confocal microscope (ImarisViewer software, version 10.2.0). qPCR data were acquired using Sequence Detection Systems Software (Version 1.9.1).
Data analysis	For images analysis: FIJI (ImageJ2 version 2.9.0/1.53t), Aperio ImageScope (version 12.3.3). For WGS analysis: nf-core/sarek pipeline (version 3.0.2), Fastp (version 0.23.2), BWA-mem (version 0.7.17-r1188), BSgenome.Hsapiens.UCSC.hg38 (version 1.4.4), GATK4 Markduplicates (version 4.2.6.1), GATK4 BaseRecalibrator (version 4.2.6.1), GATK4 ApplyBQSR (version 4.2.6.1), nf-core/circdna (version 1.0.1), cnvkit (version 0.9.9),AmpliconSuite-Pipeline (https://github.com/jluebeck/AmpliconSuite-pipeline),AmpliconArchitect (version 1.3_r1), AmpliconClassifier (version 0.4.11), cnvkit (version 0.9.9), PURPLE (version 3.8.1),AMBER (version 1.14), COBALT (version 3.9). For circle-seq analysis: cutadapt (version 3.4), BWA Mem (version 0.7.17-r1188), deeptools 'bamCoverage' (version 3.5.1), genomation (version 1.2.6). For droplet digital PCR: QuantaSoft (version 1.3.2.0). For barcode sequencing analysis: BWA (version 0.7.18), BWA Mem (version 0.7.17-r1188), Rsubread (version 2.18.0). RNA-seq analysis: STAR (version 2.7), RSEM (version 1.3.3), DESeq2 (version 1.34.0), fgsea (version 1.20.0), GSVA (version 1.42.0), msiggdbr (version 7.5.1), nf-core/rnafusion (version 3.0.0). Spatial analysis: Xenium Explorer (version 3.1.0), Seurat (version 5.1.0), presto (version 1.0.0). For statistical analysis: R (v4.1.2) or GraphPadPrism (v9.5.1).

For manuscripts utilizing custom algorithms or software that are central to the research but not yet described in published literature, software must be made available to editors and reviewers. We strongly encourage code deposition in a community repository (e.g. GitHub). See the Nature Portfolio guidelines for submitting code & software for further information.

Data

Policy information about availability of data

All manuscripts must include a data availability statement. This statement should provide the following information, where applicable:

- Accession codes, unique identifiers, or web links for publicly available datasets
- A description of any restrictions on data availability
- For clinical datasets or third party data, please ensure that the statement adheres to our policy

All processed data generated for this study are provided in the Supplementary tables. RNA-seq data have been deposited in the GEO database under accession code: GSE247129. Barcode sequencing data have been deposited in the GEO database under accession code: GSE281325. WGS and CIRCLE-seq data generated in this study have been deposited in the European Genome-phenome Archive (EGA) hosted by the EBI and CRG, under accession number EGAS50000000193 (https://ega-archive.org/studies/EGAS50000000193) and EGAS50000000194 (https://ega-archive.org/studies/EGAS50000000194), respectively. Spatial transcriptomics data have been deposited in the Zenodo database: DOI 10.5281/zenodo.14051631.

Research involving human participants, their data, or biological material

Policy information about studies with human participants or human data. See also policy information about sex, gender (identity/presentation), and sexual orientation and race, ethnicity and racism.

Reporting on sex and gender	Research findings do not apply to one sex only. The sex of each patient was collected by consent and self-reported. Information regarding sex is provided in Supplementary Table S1. For WGS, organoids from 39 unique patients were included: 20 females, and 19 males. No gender-based analyses are shown and no significant associations with sex were observed. All source data comprise a patient identifier to disaggregate data based on sex.
Reporting on race, ethnicity, or other socially relevant groupings	Data on race and ethnicity of patients were not collected.
Population characteristics	Organoids were derived from patients with histologically verified pancreatic cancer, without distant metastases, who underwent surgical resection with stored normal tissue, cryopreserved and/or FFPE sections, with complete clinical and pathological data and follow up data for at least 24 months. For two patients, organoids were derived also from the matched lymph node metastases. All patients were operated at the General and Pancreatic Surgery Unit at the University of Verona, Italy. One patient had neoadjuvant therapy before surgery. All patient characteristics are in Supplementary Table S1.
Recruitment	Patients undergoing pancreatic cancer surgery resection were recruited by referring physician. No self-selection biases have been identified.
Ethics oversight	The fresh tissues used to establish organoids were collected under a study approved by the Integrated University Hospital Trust (AOUI) Ethics Committee (Comitato Etico Azienda Ospedaliera Universitaria Integrata): approval number 1911 (Prot. n 61413, Prog 1911 on 19/09/2018). Formalin-fixed and paraffin-embedded tissues were collected under protocol number 1885 approved by the AOUI Ethics Committee and retrieved from the ARC-NET Biobank.

Note that full information on the approval of the study protocol must also be provided in the manuscript.

Field-specific reporting

Please select the one below that is the best fit for your research. If you are not sure, read the appropriate sections before making your selection.

☒ Life sciences ☐ Behavioural & social sciences ☐ Ecological, evolutionary & environmental sciences

For a reference copy of the document with all sections, see nature.com/documents/nr-reporting-summary-flat.pdf

Life sciences study design

All studies must disclose on these points even when the disclosure is negative.

Sample size	Sample size represents number of organoids, tumor cells, or patient tissues. The sample size was not predetermined using a statistical method; instead, it was determined based on our experience with the relevant experiments and similar published studies. Sample sizes for each experiment are provided in the Figure or in the Figure legends.
Data exclusions	No data was excluded
Replication	The number of biological or technical replicas for each experiment is indicated in the figure or in the figure legends.
Randomization	All experiments performed involved the use of organoids or patients' tissues. Therefore, randomization was not relevant for this study.
Blinding	Blinding was not applicable as all conditions were labelled for data collection. The entire experimental process and subsequent data analysis were conducted using standardized protocols, objective quantitative methods or have been validated with orthogonal techniques.

Reporting for specific materials, systems and methods

We require information from authors about some types of materials, experimental systems and methods used in many studies. Here, indicate whether each material, system or method listed is relevant to your study. If you are not sure if a list item applies to your research, read the appropriate section before selecting a response.

Materials & experimental systems

n/a	Involved in the study
☐	☒ Antibodies
☐	☒ Eukaryotic cell lines
☒	☐ Palaeontology and archaeology
☒	☐ Animals and other organisms
☒	☐ Clinical data
☒	☐ Dual use research of concern
☒	☐ Plants

Methods

n/a	Involved in the study
☒	☐ ChIP-seq
☒	☐ Flow cytometry
☒	☐ MRI-based neuroimaging

Antibodies

Antibodies used

The following antibodies were used:
c-MYC (Abcam, clone Y69, cat #ab32072, lot#1012026-1, for WB dil 1:1000, for IF dil 1:500),
c-MYC (Biocare, clone EP121, cat #ALI 415 G7, for IHC),
GATA6 (R&D Systems, polyclonal, cat #AF1700, for IHC dil 1:200),
ΔNp63 (Leica, clone BC28, cat #PA0163, for IHC ready-to-use),
CK5 (Novocastra, clone XM26, cat #PA0648, for IHC dil 1:100),
γ-H2AX (eBioscience, clone CR55T33, cat #14-9865-82, lot#1968333, for IF 1:500),
γ-H2AX (Abcam, clone EP854(2)Y, cat# ab81299, lot#GR3203642-4, for WB dil 1:1000),
GFP (Cell Signaling Technologies, clone D5.1, cat#2956, lot# 6, for WB dil 1:1000),
GAPDH (Cell Signaling Technologies, clone D16H11, cat# 5174, lot#6, for WB dil 1:5000),
Histone H3 (Sigma-Aldrich, polyclonal, cat#09-838, lot#2698469, for WB dil 1:5000).
Alexafluor488 Donkey anti-mouse (Invitrogen, cat#A21202, lot#1423052, for IF dil 1:500)
AlexafluorPlus555 Goat anti-rabbit (Invitrogen, cat#A32732, lot#VC297826, for IF dil 1:500)
Alexafluor647 Goat anti-rabbit (Invitrogen, cat#A21245, lot#2833435, for IF dil 1:500)
Peroxidase-conjugated AffiniPure donkey anti-rabbit (Jackson Immunoresearch Laboratories, polyclonal, cat#711-035-152)

Validation

Each antibody was validated according to manufacturer's instruction.
• c-MYC, cat#ab32072: https://www.abcam.com/products/primary-antibodies/c-myc-antibody-y69-chip-grade-ab32072.pdf
• c-MYC, cat #ALI 415 G7: https://biocare.net/wp-content/uploads/PDF%20Data%20Sheets/415.pdf
• GFP, cat#2956: https://www.cellsignal.com/products/primary-antibodies/gfp-d5-1-rabbit-mab/2956
• GATA6, cat#AF1700: https://resources.rndsystems.com/pdfs/datasheets/af1700.pdf
• ΔNp63, cat#PA0163: https://shop.leicabiosystems.com/en-de/ihc-ish/ihc-primary-antibodies/pid-p40
• CK5, cat#PA0648: https://shop.leicabiosystems.com/en-de/ihc-ish/ihc-primary-antibodies/pid-cytokeratin-5
• γ-H2AX, cat# 14-9865-82: https://www.thermofisher.com/order/genome-database/dataSheetPdf?producttype=antibody&productsubtype=antibody_primary&productId=50-9865-42&version=345-
• γ-H2AX, cat# ab81299: https://www.abcam.com/en-it/products/primary-antibodies/anti-gamma-h2ax-phospho-s139-antibody-ep8542y-ab81299
• GAPDH, cat# 5174: https://www.cellsignal.com/products/primary-antibodies/gapdh-d16h11-xp-rabbit-mab/5174
• Histone H3, cat# 09-838: https://www.merckmillipore.com/IT/it/product/Anti-Histone-H3.3-Antibody,MM_NF-09-838
• Alexafluor488 Donkey anti-mouse, cat#A21202: https://www.thermofisher.com/antibody/product/Donkey-anti-Mouse-IgG-H-L-Highly-Cross-Adsorbed-Secondary-Antibody-Polyclonal/A-21202
• AlexafluorPlus555 Goat anti-rabbit, cat#A32732: https://www.thermofisher.com/antibody/product/Goat-anti-Rabbit-IgG-H-L-Highly-Cross-Adsorbed-Secondary-Antibody-Polyclonal/A32732
•Alexafluor647 Goat anti-rabbit, cat#A21245: https://www.thermofisher.com/antibody/product/Goat-anti-Rabbit-IgG-H-L-Highly-Cross-Adsorbed-Secondary-Antibody-Polyclonal/A-21245
• Peroxidase-conjugated AffiniPure donkey anti-rabbit, cat#711-035-152:https://www.jacksonimmuno.com/catalog/products/711-035-152

Eukaryotic cell lines

Policy information about cell lines and Sex and Gender in Research

Cell line source(s)	HEK293T cell line were purchased from ATCC.
Authentication	Commercially available cell lines are authenticated by STR profiling.
Mycoplasma contamination	Cells routinely tested negative for mycoplasma contamination.

Commonly misidentified lines (See ICLAC register)	The cell line used in this study was not found in the ICLAC register.

Plants

Seed stocks	*Report on the source of all seed stocks or other plant material used. If applicable, state the seed stock centre and catalogue number. If plant specimens were collected from the field, describe the collection location, date and sampling procedures.*
Novel plant genotypes	*Describe the methods by which all novel plant genotypes were produced. This includes those generated by transgenic approaches, gene editing, chemical/radiation-based mutagenesis and hybridization. For transgenic lines, describe the transformation method, the number of independent lines analyzed and the generation upon which experiments were performed. For gene-edited lines, describe the editor used, the endogenous sequence targeted for editing, the targeting guide RNA sequence (if applicable) and how the editor was applied.*
Authentication	*Describe any authentication procedures for each seed stock used or novel genotype generated. Describe any experiments used to assess the effect of a mutation and, where applicable, how potential secondary effects (e.g. second site T-DNA insertions, mosiacism, off-target gene editing) were examined.*